Influence of the Arrangement of the Cells/Modules of a Traction Battery on the Spread of Fire in Case of Thermal Runaway

Ana Olona and Luis Castejón *

Posted Date: 4 December 2023

doi: 10.20944/preprints202312.0101.v1

Keywords: Thermal Runaway; pouch cell; chemical composition analysis; structural analysis; thermal failure test

Article

Influence of the Arrangement of the Cells/Modules of a Traction Battery on the Spread of Fire in Case of Thermal Runaway

A. Olona [1] and L. Castejón [2,*]

[1] Research Department, Electric Vehicle and Mobility Area, Instituto de Investigación sobre Vehículos, S.A., Ctra. N232, km 273, 50690 Pedrola, Zaragoza, Spain; a.olona@centro-zaragoza.com

[2] Department of Mechanical Engineering. University of Zaragoza, C/María de Luna s/n, 50018 Zaragoza, Spain

* Correspondence: luiscast@unizar.es; Tel.: +34976762556

Abstract: When designing the battery of an electric vehicle, different parameters must be considered to obtain the safest arrangement of the battery/modules/cells from the mechanical and thermal point of view. In this study, the thermal runaway propagation mechanism of lithium-ion cells is analyzed as a function of their arrangement within a battery pack in case of a fire propagation of a battery pack in which a thermal runaway has occurred. The objective is to identify which cell/module arrangement is most critical within the battery pack by microscopic analysis of the structure and chemical composition of the most damaged cells, both horizontally and vertically, of a battery belonging to a burnt vehicle. And their final condition has been compared with the condition of new cells of the same type. In this way the structure and chemical composition of the anode, cathode and separator after Thermal Runaway has been compared. This research has been carried out to obtain information to understand the mechanical properties of lithium-ion cells and their behavior after thermal runaway heating leading to the propagation of a fire. Through the analysis carried out, it is concluded that cells placed in a vertical arrangement have worse behavior than cells in a horizontal arrangement. Regarding the safety of the battery, the results of this study will allow to determine which arrangement and structure of the cells within the battery pack is safer against thermal runaway due to thermal failure.

Keywords: Thermal Runaway; pouch cell; chemical composition analysis; structural analysis; thermal failure test

1. Introduction

Battery fire safety remains a major concern due to their low temperature stability [1]. Over the past 30 years, there has been many accidents involving lithium-ion batteries, indicating that those batteries are not fire-safe. In addition, there have been several serious fire accidents in Tesla Model S electric vehicles [2–4,6,7]. Some caught fire while driving and others during the charging and discharging process.

In general, lithium-ion batteries are most vulnerable when subjected to temperature, electrical failure, or mechanical impact [8]. Lithium-ion batteries have limited temperature and voltage threshold, and their components are unstable. Namely, the electrolyte is flammable, and the electrodes are made of a material with a high specific energy. All these characteristics imply this type of cell prone to Thermal Runaway (TR) in some abusive cases [9,10].

A lithium-ion battery can fail due to mechanical, electrical, or thermal failures at the cell, module, or battery pack level (Figure 1). These failures occur as a successive series, leading to the phenomenon of TR. Thermal failure can occur due to overheating, which can be caused by incorrect contact connections or excessive heat in the vicinity of the battery pack, such as from a fire caused by a car accident. In addition, overheating can occur during fast charging with a supercharger. This failure can also be caused by an internal short circuit, which occurs due to cell separator failures, contamination, manufacturing defects or dendrite formation (lithium build-up) on the anode. This failure can also occur due to defects during cell manufacturing that cause an internal short circuit.

Preprints (www.preprints.org) | NOT PEER-REVIEWED | Posted: 4 December 2023 doi:10.20944/preprints202312.0101.v1

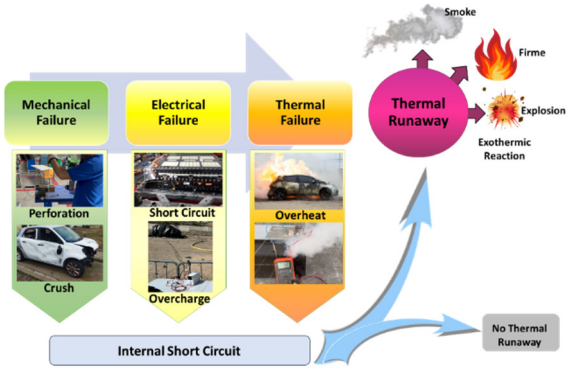

Figure 1. Thermal runaway mechanism of lithium-ion battery for EVs [11].

Thermal abuse failure due to external heat or flame exposure, also due to heat build-up inside due to incorrect removal of reaction heat or initiation of unwanted internal exothermic reactions, can lead to Thermal Runaway. Controlled fire tests carried out on a complete electric vehicle with an installed high-voltage battery, such as scale tests with different cells and different cell arrangements, will allow characterization of the behavior of the cells in a fire due to electrical failure, high temperature or significant deformation. The Thermal Runaway reaction is influenced by the stranded energy, as the energy that remains stored inside the lithium-ion battery even after it has been discharged to a certain extent. In the context of a fire involving a lithium-ion battery, the stranded energy can represent a significant risk. To handle safely a lithium-ion battery involved in a fire, it is important to be aware of the potential for trapped energy and to ensure that the battery is fully discharged and cooled before attempting to handle or transport it.

If a high-voltage battery is damaged, energy remains inside any undamaged battery modules and cells, with no way to discharge it. That stranded energy can cause a high-voltage battery to reignite multiple times after firefighters extinguish an electric vehicle fire. Emergency responders have no way of measuring how much energy remains in a damaged battery, and no way of draining that energy, other than such time-consuming and risky methods as allowing a battery fire to burn itself out. Engineers or other specialists can use the battery management system to check the remaining voltage if the system is operational, and some batteries have built-in discharge ports, also for use by specialists. However, the high-voltage battery system can be damaged in a crash, preventing access to the battery management system or to the discharge ports. The duration of the post-crash fire and the multiple battery reignitions would be the evidence that the battery contained stranded energy. Several researchers [12] from Oak Ridge National Laboratory conducted a study in which he concluded that lithium-ion cells with SOC>80 % subjected to mechanical damage were more prone to thermal runaway while cells with low SoC would not suffer thermal runaway but they only would experience a slight temperature rise.

Several studies have been conducted to analyze the behavior of lithium-ion cells under external heating conditions. Huang et al [13] heated with an electric heater three 50 Ah lithium-ion cells at different SoCs (States of Charge) and concluded that the cell only turned on when the cell surface reached 112 to 121 °C. The cell response and thermal runaway characteristics depend on the SoC. If the SoC is increased, then the time from heating to ignition is gradually reduced [13–15] and the reactions become more dangerous. Feng et al [16] divided the internal chemical reactions occurring in lithium-ion batteries into different stages depending on the temperature reached. When lithium-ion batteries are overheated, their temperature gradually increases. The SEI (solid electrolyte interphase) film begins to decompose when the cell reaches 90-130 ◦C, [17]. As the SEI decomposes, the electrolyte reaches more easily the graphite surface and readily reacts with the intercalated lithium to release oxygen and generate more heat [18]. On the other hand, polyethylene (PE) can melt at 130-140 ◦C, causing an internal micro-short circuit and thus a continuous increase in battery temperature [19]. When the temperature reaches around 200 ◦C the cathode materials start to

 doi:10.20944/preprints202312.0101.v1

decompose and release oxygen [20]. In addition, the decomposition reaction of the SEI film and the chemical reaction between the electrolyte and the cathode metal oxide materials is accelerated, as well as the reaction between the electrolyte and the negative active substances, which will produce more heat and gases [15] such as oxygen, CO, HF and NO [21–25]. As the temperature increases, the internal chemical reaction of the cell becomes increasingly intense and complex, generating a large amount of heat and combustible gases [26], followed by a thermal runaway reaction, causing the lithium-ion cell to burn or even explode.

It is important to understand the risk/hazard for the design of single cells and battery packs and modules to avoid or minimize the impact of thermal runaway. However, there are few studies on methods of assessing the cells or battery modules safety. Several studies have analyzed the influence of cell arrangement in a lithium-ion battery pack on Thermal Runaway (TR) propagation in both open and enclosed space [27]. Experimental results show that when the battery SoC is 100% and the spacing is more than 4 mm in the horizontal direction and 8 mm in the vertical direction in a closed environment that the possibility of thermal propagation for the battery pack is higher than that in an open environment. It is concluded that the propagation possibility of the battery pack in vertical arrangement is higher than in horizontal arrangement. Studies indicate that TR only occurs when the SoC is higher than 50%. On the other hand, the critical spacing that triggers TR is 4 and 6 mm for 80% and 100% SoC batteries respectively [28]. Feng et al. [29] conducted a mechanical failure (penetration) inducing TR on a module of 6 cells in series contact and concluded that the cell casing transfers the most heat and they developed a thermally resistant layer between the cells to prevent the propagation of TR in the module [30]. Lopez et al. [31] analysed the influence of inter-cell spacing on TR and concluded that the spacing between cells in the battery pack greatly affects TR propagation. They analysed different battery modules in series and concluded that the key to TR propagation is heat conduction. Therefore, there are several studies on the propagation of TR in series-connected battery modules [29–31] but there are few studies to analyse the propagation of TR in parallel-connected battery modules. Wike et al. [32] stated that the temperature increase after TR in a parallel connected battery cell module is higher than if the cells in the module are connected in series. Lamb et al. [33] also found that the temperature rise in a module with parallel connected cells was higher and the TR propagation was accelerated. Gao et al. [34] carried out a study of the propagation of TR in a large format battery module with parallel connections, 18 pouch cells in parallel 24 Ah. It is observed that the undamaged cells transfer current to the cell experiencing TR, which causes it to experience a 10°C higher temperature compared to a module with the cells connected in series. Therefore, a module with parallel connections is less safe.

In this study, overheating tests of a lithium-ion battery in an electric vehicle have been carried out using a fossil fuel heater to analyze how the arrangement of the cells influences the propagation of Thermal Runaway. The Authors hope that this research can provide useful conclusions for the improvement of the Li-ion cells arrangement in the electric vehicle with the aim of reducing the damage caused by Thermal Runaway in lithium-ion batteries in automotive applications.

2. Materials and Methods

2.1. Methodology

The goodness of the results obtained will depend on the ability of the cell tests to reproduce the real behaviour of a battery pack. As a starting point, a controlled fire test with a vehicle fitted with a battery pack was carried out aimed to characterise its behaviour.

2.1.1. Controlled Fire Test of an Electric Vehicle

Firstly, a controlled fire test was carried out on a complete electric vehicle, specifically a Nissan Leaf, in which the temperature evolution and the behavior of the battery were analyzed. The fire was started by positioning a fuel burner on the bottom of the vehicle battery. Time and the temperature of the battery were monitored through the test with the help of a thermographic camera. The following table 1 shows the main characteristics of the battery analyzed.

Preprints (www.preprints.org) | NOT PEER-REVIEWED | Posted: 4 December 2023 doi:10.20944/preprints202312.0101.v1

Table 1. Characteristics of the battery of the burnt Nissan Leaf vehicle.

Vehicle	Battery Electric Vehicle
Date of first registration	17/12/2015
Range	121 km (EPA test)
Battery specifications	
Capacity	24 kWh
Battery Voltage	360 V
Battery	Lithium-ion battery
Cell type	Laminate type, pouch cells
Cathode Active Material	LMO ($LiMn_2O_4$) with LNO ($LiNiO_2$)
Anode Active Material	Graphite
Capacity	32,5 Ah
Nominal Voltage	3,75 V
Battery Modules	48
Cells per module	4
Energy Density	157 Wh/kg
Battery Weight	~180 kg
Battery Price	7.000 €
State of Charge (SoC)	68,0%

The test started and the vehicle was getting hotter and hotter as the combustion process progressed. Within 3 minutes from the start of the test, the battery pack reached a temperature close to 805ºC. It was not until about eight minutes from the begging that small explosions from the vehicle airbag gas generators began to be heard, followed by the phenomenon of thermal runaway in the battery cells.

Initially the fire was extinguished using a fire blanket. After just over ten minutes from the start of the test, the temperature in the battery area exceeded 1,000 °C. It was at this point that the firefighters proceeded to cover the vehicle with the blanket. Immediately after the vehicle had been covered by the blanket, the surface temperature of the vehicle dropped from approximately 850°C to about 350°C. From this moment on, the blanket insulates from the radiation emitted by the fire, preventing from spreading any element into the environment and at the same time cooling the vehicle. In addition, the blanket prevents the oxygen supply, preventing the fire from continuing when all the oxygen confined under the blanket is consumed.

Figure 2. Zaragoza City Council firefighters covering the burnt vehicle with the fire blanket.

Preprints (www.preprints.org) | NOT PEER-REVIEWED | Posted: 4 December 2023 doi:10.20944/preprints202312.0101.v1

As the minutes passed, the temperature recorded by the thermal imaging camera was dropping to around 100ºC. However, electric vehicle fires have a high risk of fire reignition because the battery continues to produce all the elements necessary for the fire to start. Namely heat, fuel and oxygen. If the vehicle is covered by the blanket there is no risk, as it is only a matter of time before the battery temperature drops. But if the vehicle is uncovered, the risk of a restart is very high. That is why after 9 minutes after the vehicle was completely covered, it was decided to remove the blanket to show how the process of restarting the fire is reproduced. Just after removing the blanket, it can be seen how the fire restarts from the battery area and quickly spreads again throughout the vehicle.

Continuing with the test, the fire increased again the temperature during the following two and a half minutes, reaching a peak temperature of around 600 ºC. Once this temperature is reached, the vehicle is covered again to insulate and extinguish the vehicle fire again, given that the blanket is reusable.

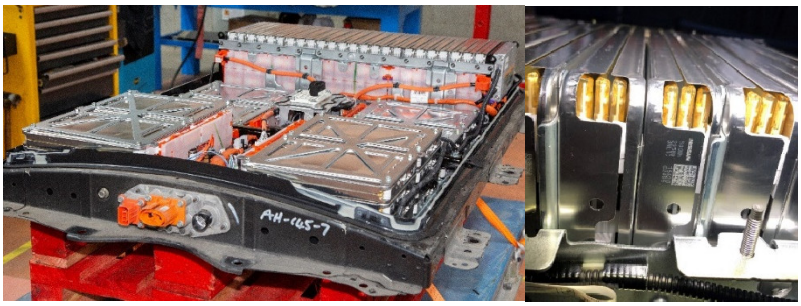

(a) **(b)**

Figure 3. a. Battery Pack before fire test. b. Detail of a battery module constructed with a 4-cell configuration).

To finalize the test, once the blanket was removed, the battery was cooled with water and the vehicle was left in quarantine to check that the fire did not restart.

Table 2. Characteristics of the controlled fire test carried out on the Nissan Leaf vehicle.

FIRE TEST SPECIFICATIONS	
Place and date	Zaragoza, 05.12.2019
Vehicle under test	Battery Electric Vehicle
TEST	
Vehicle	Vehicle only with voltage battery
Fire	Ignition Burners (fossil fuel)
Method to extinguish the fire	Bridgehill Car Fire Blanket
Temperature monitoring	Thermal Imaging Infrared Camera: FLIR T640
Thermal Imaging Infrared camera distance	13,7 m
Ambient Temperature	7,1 ˚C
Average Wind Speed	2,5 m/s
Maximum Wind Speed	8,9 m/s
Maximum Temperature reached	~1000 ˚C
Time to start Battery Thermal Runaway	~8 min
After removing the blanket	
Amount of water to extinguish the fire	400 l

Images of the electric vehicle fire test are shown below:

Preprints (www.preprints.org) | NOT PEER-REVIEWED | Posted: 4 December 2023 doi:10.20944/preprints202312.0101.v1

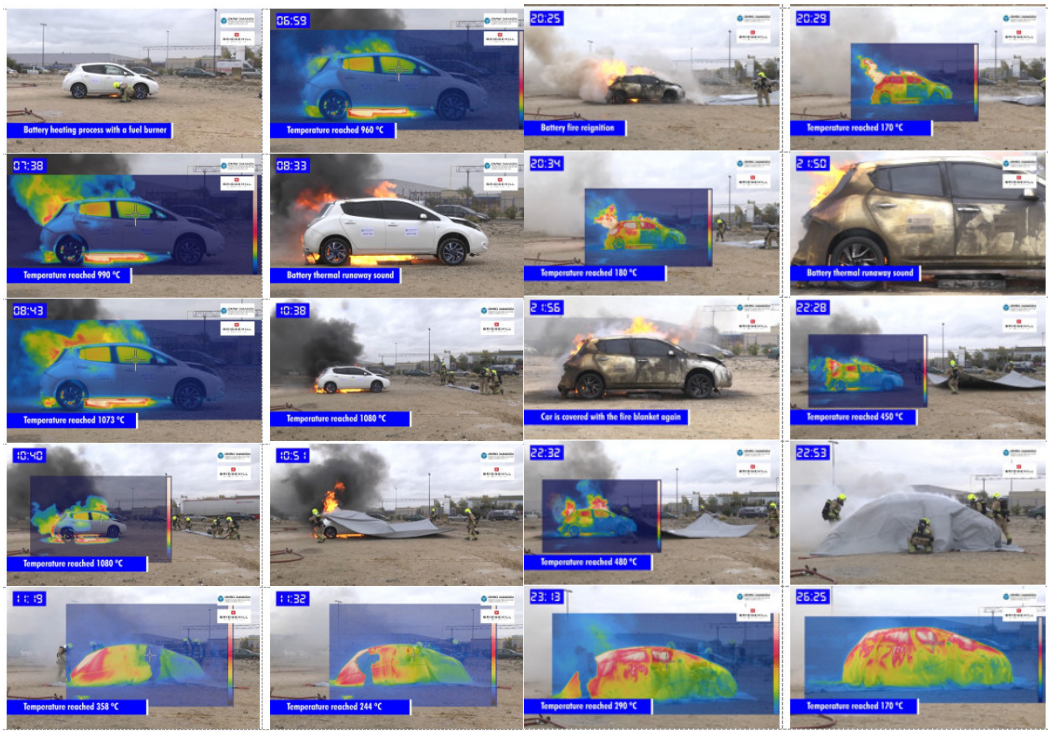

Figure 4. Images of the controlled fire test carried out on the Nissan Leaf vehicle under study.

2.1.2. Identification of the most damaged cells in the analysed battery

Once the test had been carried out and the necessary quarantine time had elapsed, the cells were dismantled to see how they behaved and their condition according to the position they were in. The aim was to analyze how the enclosure was damaged, according to the position of each cell within the enclosure. Moreover, deformation suffered by each of the cells was studied. Finally, the condition of these cells has been perfectly documented.

Figure 5. Pictures of the state of the battery pack, the module, and the lithium-ion cells inside the battery pack.

Once the burnt battery of the Nissan Leaf had been disassembled, the most damaged modules were identified, both vertically (module 11) and horizontally (module 30), and all modules were disassembled and visually analyzed.

Preprints (www.preprints.org) | NOT PEER-REVIEWED | Posted: 4 December 2023 doi:10.20944/preprints202312.0101.v1

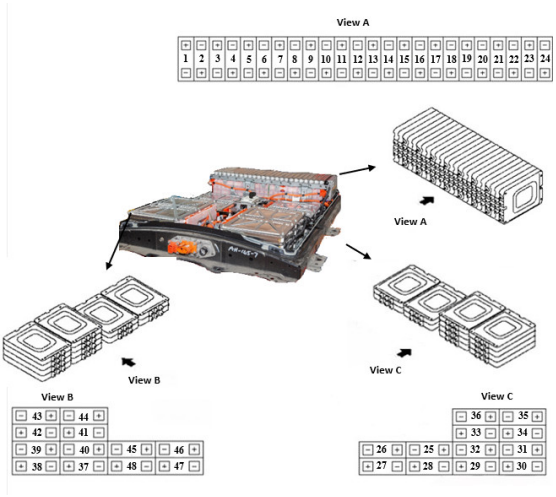

Figure 6. Exploded view and module identification of the traction battery of a first-generation Nissan Leaf.

Figure 7. Burnt Nissan Leaf battery disassembled in the arrangement in which it is in the vehicle.

The following pictures show the state of the most damaged modules:

Figure 8. Images of the condition of module 30 (horizontal arrangement) of the battery pack of the burnt Nissan Leaf vehicle. This module has been identified as the most damaged between the modules in the horizontal arrangement.

Preprints (www.preprints.org) | NOT PEER-REVIEWED | Posted: 4 December 2023 doi:10.20944/preprints202312.0101.v1

Figure 9. Images of the condition of module 11 (vertical arrangement) of the battery pack of the burnt Nissan Leaf vehicle. This module has been identified as the most damaged between the vertically arranged modules.

The following figure identifies the position of the most damaged modules in the battery pack analyzed:

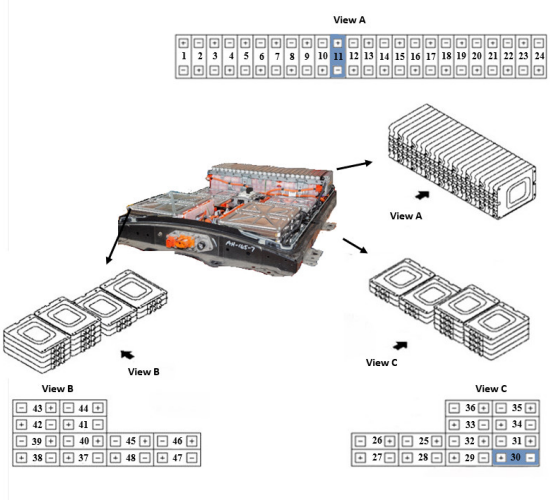

Figure 10. Exploded view of the first-generation Nissan Leaf battery, with identification of the most damaged modules, shaded in blue.

2.1.3. Generation of Samples for Cross-Sectional and Structural Analysis

A study of the structure was carried out by taking samples and analyzing them transversally (there are several layers of anodes and cathodes, as well as separators. It is a stack sample of materials), and on the other hand, a surface analysis of the chemical composition was carried out. To do that anode, cathode and separator were separated.

For the structure analysis test, three transversal section samples were taken from a cell of module 11, three transversal section samples from a cell of module 30 and two transversal section samples from a new cell. For chemical composition and morphology analysis, one sample was taken from the cathode, one sample from the anode and one sample from the separator for module 11, module 30 and the new cell, respectively. The samples for the tests were obtained at Centro Zaragoza facilities, and once the samples had been obtained, the tests were carried out at the Material Science Department of the University of Zaragoza. Sampling has been carried out considering the indications of a previous study [35]. Images from sample preparation to Sibe tested for the new cell are shown below.

Preprints (www.preprints.org) | NOT PEER-REVIEWED | Posted: 4 December 2023 doi:10.20944/preprints202312.0101.v1

a) b) c) d)

Figure 11. Obtaining the sample for surface analysis. a) Image of the inside of a pouch cell from where the samples for surface analysis of the stacked layers (anode, cathode, and separator in the case of the intact cell) have been obtained, b) Sample generated from the anode (copper tab), c) Sample generated from the cathode (aluminum tab), d) Sample generated from the separator.

a) b) c)

Figure 12. Sample and obtaining the sample for structural analysis. a) Location of the points from where the samples have been obtained for the structural analysis of the stacked layers: 1. Anode tab (copper), 2. Cathode tab (aluminum), 3. b) Sample generated in position 3, c) Section of the pouch cell once the sample has been extracted.

Figure 13. Obtaining samples from a module 30 calcined cell.

For the preparation of the surface sections of the individual layers, after obtaining the samples, with a surface area of approximately 5 mm x 5 mm, of each of the different layers of the cell, anode, cathode and separator (in the case of the new cell), they were coated with a layer of high purity carbon of 10.40 nanometer thick carbon layer to make them conductive, using a Leica EM ACE600 sputtering coater, and placed on an aluminum support with a double-sided carbon adhesive tape so that they do not move from the support during the analysis. A small sample of cobalt is placed to calibrate the equipment.

After obtaining the samples, with a surface area of approximately 10 mm x 10 mm, from the electrode stack, the samples are embedded in resin to facilitate handling and improve the preparation result, and then polished so that the surface is scratch and deformation free, flat, and highly reflective. A prepared sample embedded in resin is shown below.

Preprints (www.preprints.org) | NOT PEER-REVIEWED | Posted: 4 December 2023 doi:10.20944/preprints202312.0101.v1

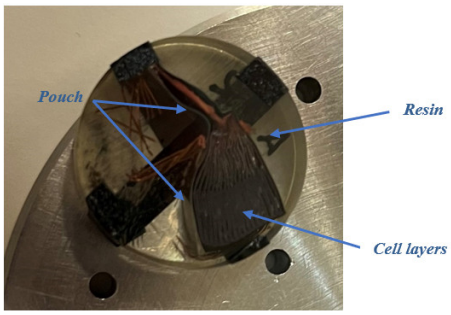

Figure 15. Layer structure of a resin-embedded and polished cell, used to identify cell parameters and cell structure.

2.1.4. Method for carrying out the surface and structural analysis

A Carl Zeiss MERLINTM Field Emission Scanning Electron Microscope (FESEM) was used to perform the analyses. It has a hot-field emission electron emission cannon and allows observations up to 0.8 nm spatial resolution and acceleration voltages between 0.02 and 30 kV. It has secondary and backscattered electron detectors in the chamber and in the column (in-lens). It also has an EDS detector for analysis of the energy of X-Max scattered X-rays (20mm^2) with SDD (Silicon Drift Detector) from Oxford Instruments. The interaction products most frequently used for the generation of images in scanning electron microscopy are secondary electrons (SEs) and backscattered electrons (BSEs). For the separation and detection of SEs and BSEs one must consider two parameters: Energy and angle distribution. For that purpose, an energy selective backscattered detector (EsB) and an angle selective backscattered detector (AsB®) have been used. The standard detectors are: In-lens detector (annular SE detector), detects SE signals and it is uses to analyze surface structure, and the SE2 detector (Everhart-Thornley type), detects SE2 signals and it is uses to analyze topography.

Morphology can be analyzed with SE2 and In Lens, and backscattered, low-energy backscattered EsB (different gray level due to different chemical composition) and high-energy backscattered AsB.

Table 3. Information on the different detectors used by the FSEM.

Standard detectors	**Detected signals**	**Typical application**
In-Lens detector (annular SE detector)	SE	Surface Structure
SE detector (Everhart-Thornley type)	SE2	Topography
Optional detectors	**Detected signals**	**Typical application**
EsB® detector with filtring grid (in-column detector)	BSE	Pure material contrast
AsB® detector, integrated	BSE	Channeling contrast (cristal orientation), compositional contrast

The SE2 detector is a Everhart-Thornley type detector. It detects SEs as well as BSEs. Electrons moving to the detector are attached by the collector and directed to the scintillator. The collector voltage (suction voltage) can be varied in the range between -250 V ad +400V. This collector voltage generates an electrical field in front of the detector thus directing the low energy SEs towards the scintillator. For all standard applications the collector bias should be set to +300V. The Angular selective Backscattered (AsB®) electron detector is completely integrated into the pole piece of the GEMINI® lens. This allows to image BSEs with ultra short working distance without alignment of the AsB® detector to the optical axis. This detector arrangement enables to separate between low angle BSEs and high angle BSEs. The AsB® detector is equipped with four diodes which can be controlled independently via a menu. Compositional mode produces images showing the atomic contrast of the specimen, whereas topography mode shows surface details.

Secondary electrons are inelastically scattered primary electrons with an energy <50 eV. They are emitted from the immediate surface of the incident primary electron beam, offering the best lateral

Preprints (www.preprints.org) | NOT PEER-REVIEWED | Posted: 4 December 2023 doi:10.20944/preprints202312.0101.v1

resolution in the range of several nanometres. The backscattered electrons scatter elastically in the field of the atomic nucleus. The energy ranges from >50 eV to the excitation energy. The higher the atomic number (atomic weight) of a phase or region, the more electrons are backscattered from this area of the sample (material contrast).

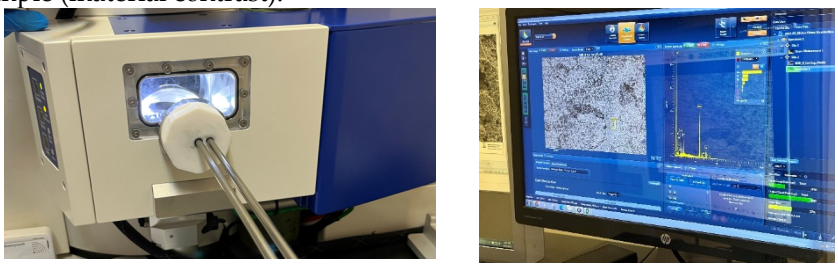

Figure 16. Views of the surface tests carried out.

2.1.5. Method for carrying out the chemical analysis

To obtain information on the chemical composition of the analysed surface, electron microscopy combined with electron energy loss spectroscopy was used. To do this, high-energy electrons were directed towards the samples, which causes the electrons in the inner shell to ionize, leaving a vacancy in the inner shell, this vacancy is occupied by an electron of a higher energy level, releasing energy that could be observed as an X-ray quantum or Auger electron (electron that is forced to leave the atom). This energy is specific to each element and is called X-ray radiation. The EDX spectra were acquired with an EDAX Super Octane silicon drift detection system (energy resolution of approximately 123 eV @ Mn Ka) equipped with a silicon nitride window for maximum sensitivity in the low-energy region.

3. Results and Discussion

The conclusions obtained from the microscopic analysis of lithium-ion cells are the basis for research into the operation, safety, and degradation of lithium-ion batteries. There are studies [35] in which analyses have been carried out using images taken under a microscope to obtain information that allows to understand the mechanical properties of lithium-ion cells. Parameters such as layer thickness, material composition, and surface properties play an important role in the analysis and further development of lithium-ion batteries. The purpose of this section is to compare the structure and chemical composition of the anode, cathode and separator in cells that have undergone Thermal Runaway, compared to an intact (new) cell.

In this section, not only the methods used to derive the surface properties and chemical composition of all the batteries, but also the results of SEM images of transverse-sections of zone 1 (Anode) of an original cell and a cell from module 11 and module 30 of the burnt Nissan Leaf vehicle battery are presented. The surface properties and chemical composition of the different components of an original cell and of a burnt cell from module 11 and module 30 are also analysed. In addition, the thickness of all battery layers is described in detail.

3.3.1. Surface Tests Results: Surface Properties and Chemical Composition Analysis

To carry out the surface analysis tests, three aluminium supports are prepared, support A, support B and support C. Two cathode samples, one from the upper cathode and one from the lower cathode, and two anode samples, one from the upper anode and one from the lower anode, are prepared in the support A from cell B of module 30, see Figure 18. Two cathode samples, one from the upper cathode and one from the lower cathode, and two anode samples, one from the upper anode and one from the lower anode, are prepared in support B from cell C of module 11, see Figure 18. And in support C, a sample of the cathode, anode and separator of a new Nissan Leaf cell is prepared.

Preprints (www.preprints.org) | NOT PEER-REVIEWED | Posted: 4 December 2023 doi:10.20944/preprints202312.0101.v1

Figure 17. View of sample preparation for surface testing.

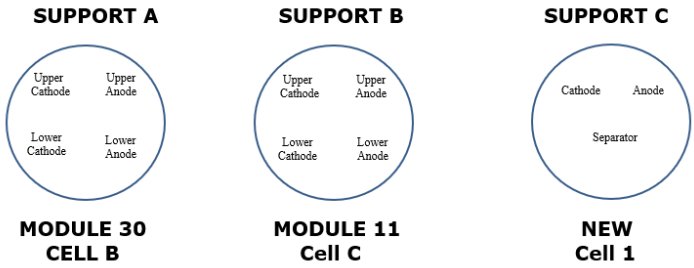

Figure 18. Arrangement of samples from different cells for surface analysis.

The following images compare different pictures obtained with FESEM of the upper cathode of module 30, module 11 and the new cell.

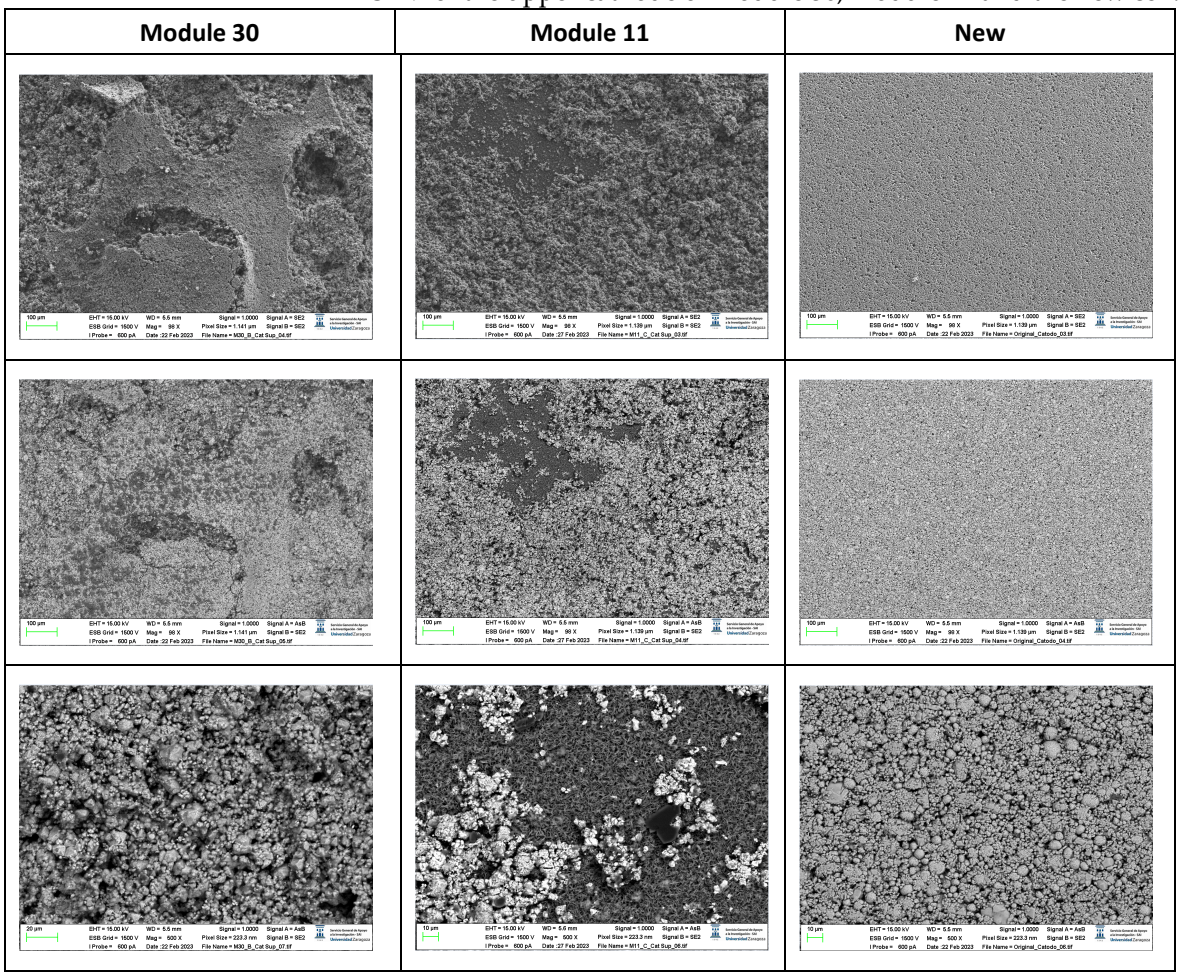

Figure 19. Comparison of images obtained with the FESEM of different areas of the upper cathode of module 30, module 11 and the new cell.

Preprints (www.preprints.org) | NOT PEER-REVIEWED | Posted: 4 December 2023 doi:10.20944/preprints202312.0101.v1

The following images compare different images obtained with FESEM of the lower cathode of module 30, module 11 and the new cell.

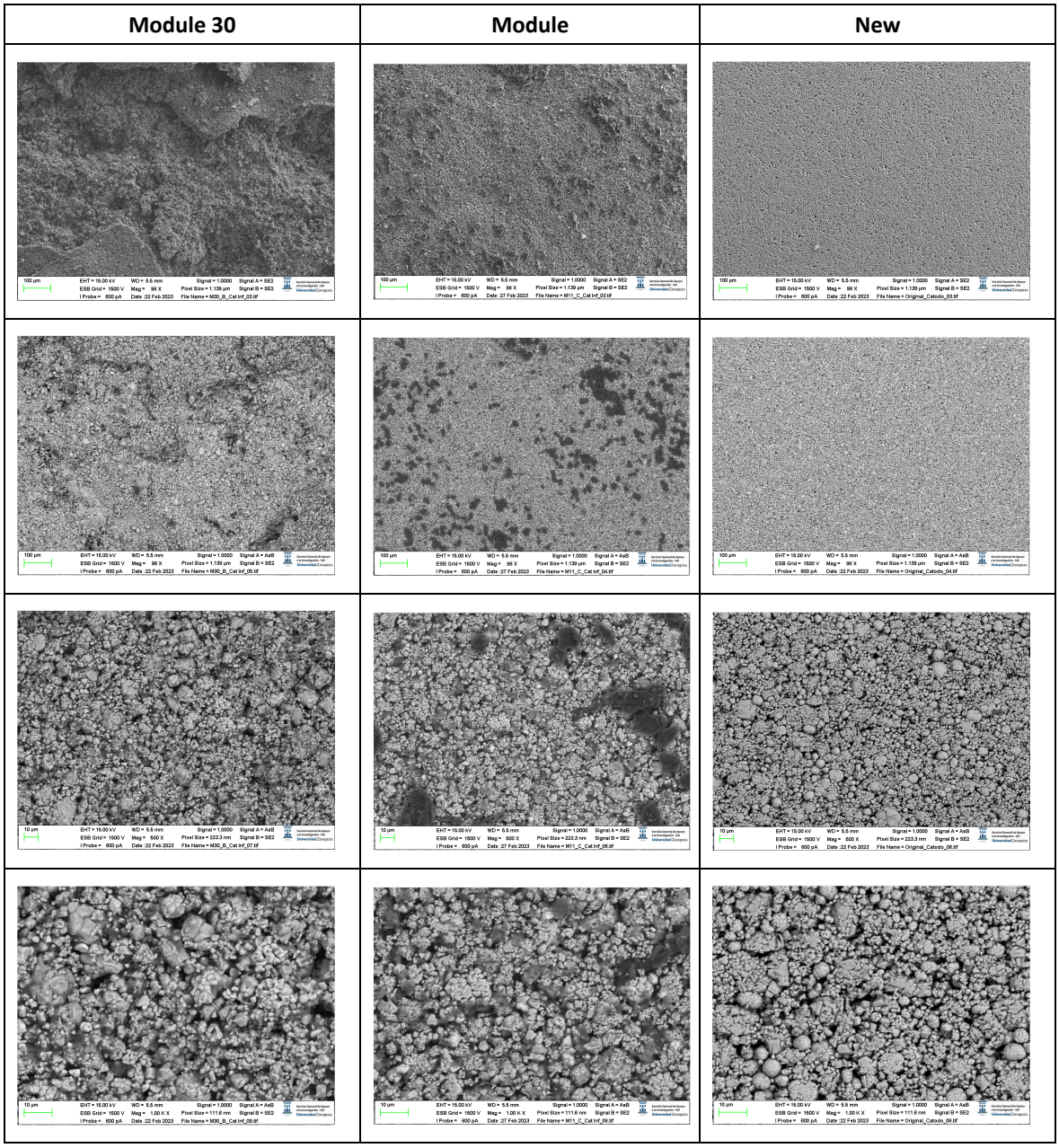

Figure 20. Comparison of images obtained with the FESEM of different areas of the lower cathode of module 30, module 11 and the new cell.

With respect to the cathode electrodes in the figure above, the cathode of an original cell has been compared with two cathodes (one upper and one lower) of module 30 and module 11 of the battery of the burning Nissan Leaf, after experiencing the Thermal Runaway. It should be noted that rather than a single particle size, most materials, especially the active materials used in battery electrodes, contain a variety of particle sizes.

It is noted that after experiencing the Thermal Runaway phenomenon, the cathode surface is covered with off-white floccules. The distribution of these floccules on the surface of the cathode electrodes is not uniform, being more concentrated in one area and more dispersed in another area.

Due to the morphology of these substances, it can be deduced that they are decomposed separators due to the high temperature, since at 150 ºC the separator shrinks and groups together. In other words, after TR the separator decomposes as the temperature increases.

Preprints (www.preprints.org) | NOT PEER-REVIEWED | Posted: 4 December 2023 doi:10.20944/preprints202312.0101.v1

The decomposition temperature of a PE-PP-based polymer is greater than 300 °C. Therefore, it is reasonable for the surfaces of the cathode electrodes to be covered with unevenly distributed separator particles.

It should be noted that the burned modules being analysed had 68% SoC (State of Charge). As SoC increases, the number of flocs increases greatly and darker coloured and spherical flocs appear, indicating that having an elevated SoC, the reaction temperature inside the cell is higher during TR, and the agglomeration and decomposition reactions of the separators are more intense [36].

The spherical cluster structure of the cathode active materials and the flake structure of the graphite have been destroyed after TR. The cathode and anode are joined together, and it is quite difficult to identify them. There are also irregularly shaped impurities/debris, some rectangular and some spherical, and chaotically distributed. When the temperature is increased due to the TR, the aluminium current collector of the chaotic electrode had oxidized and adhered to the anode side.

Therefore, it is normal to observe in the cathode traces of fragments of cathode materials after TR, ash from the cathode material and separators, products of exothermic reactions and graphite peels.

It is observed that in the case of module 11 there are more dark-coloured flocs than in the case of module 30, and there are more in the upper cathode than in the lower cathode. Therefore, it is concluded that module 11, in vertical arrangement, experiences higher temperature in the TR at the same SoC as module 30, which is in horizontal arrangement. If the structural transformation (morphology analysis with InLens) of the cathode materials after the TR is analysed (Figures 21 and 22) it is observed that in the case of modules 30 and 11 with a SoC of 68% after the TR, the layered structure of the material was destroyed, the particles dispersed outside the original layered structure and adhesion occurred. The positive electrode material (cathode) reacted at high temperature and decomposed. On the other hand, carbon particles from the negative electrode (anode) were doped into the positive electrode (cathode) through the damaged diaphragm.

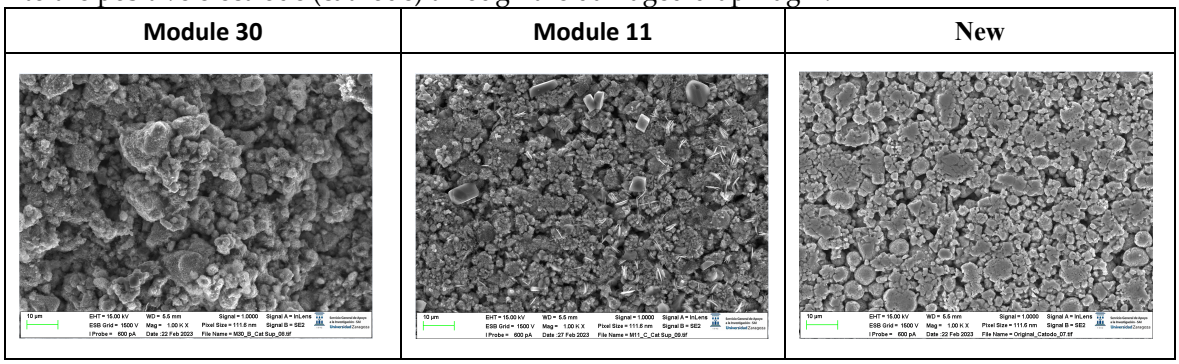

Figure 21. Morphological analysis of the transformation of the upper cathode of Module 30 and Module 11 after the Thermal Runaway compared with the initial cathode structure of a new cell.

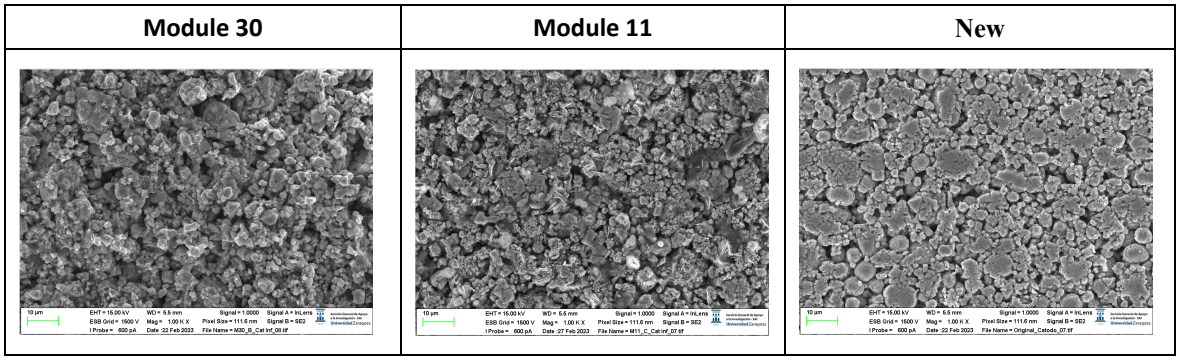

Figure 22. Morphological analysis of the transformation of the lower cathode of Module 30 and Module 11 after the Thermal Runaway compared with the initial cathode structure of a new cell.

Preprints (www.preprints.org) | NOT PEER-REVIEWED | Posted: 4 December 2023 doi:10.20944/preprints202312.0101.v1

It is observed that in the case of the lower cathode of module 30 (horizontal arrangement) the particles are smaller compared to the upper cathode of module 30, this may be due to the higher temperature as it is more exposed.

In the case of module 11 (vertical arrangement) there is no difference between the particle size of the upper cathode and the lower cathode. Hereafter, the chemical composition analysis of the upper cathode of module 30 and module 11 will be presented in comparison to the composition of the original cathode. The cathode showed a granular surface structure as can be seen in the following image (Figure 23). The largest particles were about 6 µm in size. The following chemical elements were identified by EDXS: manganese (Mn), cobalt (Co), nickel (Ni), oxygen (O), and carbon (C). This led to the conclusion of a $LiNiMnCoO_2$ (NMC) cathode chemistry. Two different types of structures were observed on the cathode surface, marked in Figure 24 by two red boxes. The results of a detailed analysis of the formed compounds show that the compound marked with "1" had the NMC chemistry mentioned above, while the second structure was determined to be a manganese oxide compound (LMO), some fluorine was also observed that may be from the electrolyte (LiPF6) when in contact with the cathode and anode. Considering these issues, cathode layer chemistry could be established as a mixture of NMC and LMO.

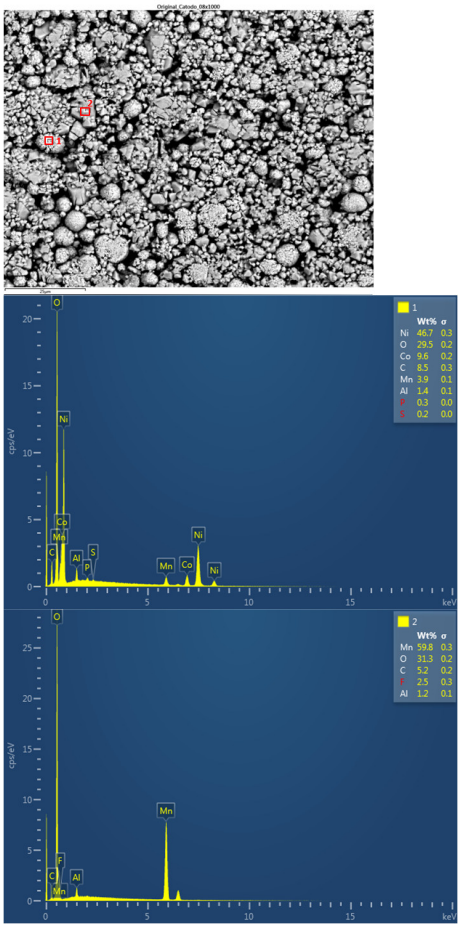

Figure 23. Chemical composition of the original cathode.

Next, the chemical composition of the upper cathode of the ignited module 30 is analyzed. The upper cathode of module 30 no longer shows a defined granular surface as in the case of the original cathode, the structure has been broken. The largest particles are about 5 µm in size. The following chemical elements were identified by EDXS: manganese (Mn), cobalt (Co), nickel (Ni), oxygen (O), fluorine (F), phosphorus (P), carbon (C) and aluminum (Al). Three different structural types were observed on the cathode surface of module 30, marked in Figure 24 by three red crosses. The results of a detailed analysis of the formed compounds show that the compound marked with "1" had the chemistry of a compound with manganese and oxygen and some fluorine and phosphorus, while it

Preprints (www.preprints.org) | NOT PEER-REVIEWED | Posted: 4 December 2023 doi:10.20944/preprints202312.0101.v1

was determined that the second structure was also a manganese and oxygen compound, more fluorine was observed than in the previous compound, was observed also nickel and aluminum. And finally in the rectangular shaped compound "3" it was observed fluorine and nickel. This last compound is due to the reactions that have taken place in the TR and that is why there are leftover of the electrolyte.

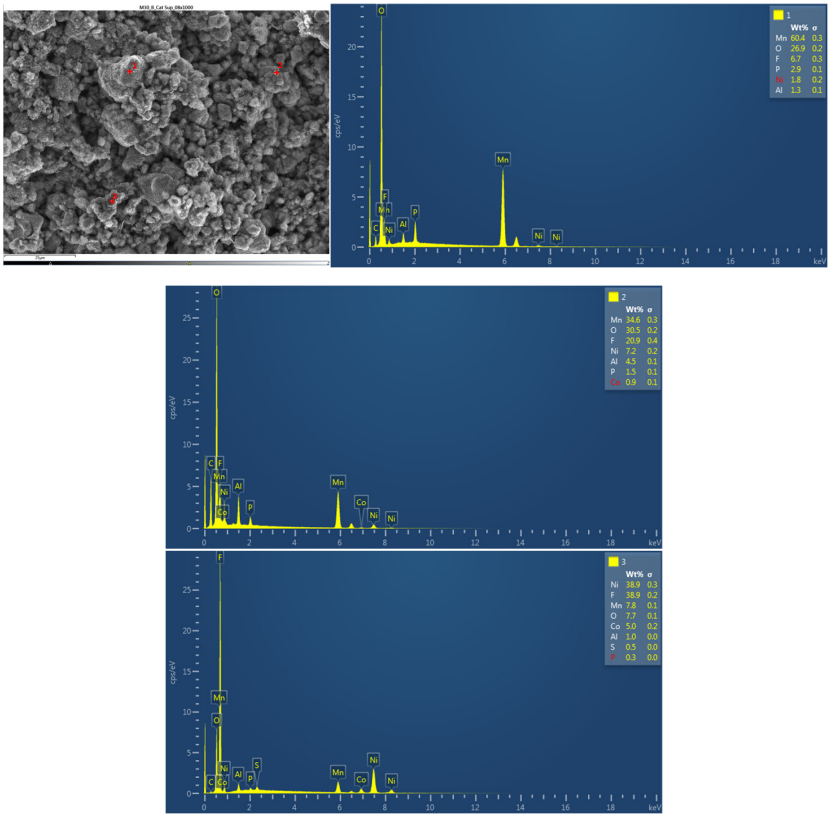

Figure 24. Chemical composition of the upper cathode of module 30.

Next, the chemical composition of the lower cathode of the ignited module 30 is analyzed. The lower cathode of module 30 also does not show a defined granular surface as in the case of the original cathode, the structure has been broken. The larger particles are about 4 μm in size, so the particles are smaller than in the case of the upper cathode of the same module, probably because they have been exposed to higher temperature values. Two different types of structures were observed on the surface of the lower cathode of module 30, marked in Figure 25 with two red crosses. The results of a detailed analysis of the compounds formed show that the compound marked with "1" had the chemistry of a compound with oxygen and manganese, while it was determined that the second structure was also the chemistry of a nickel and oxygen compound, some manganese, fluorine, cobalt, and aluminum were also observed.

Preprints (www.preprints.org) | NOT PEER-REVIEWED | Posted: 4 December 2023 doi:10.20944/preprints202312.0101.v1

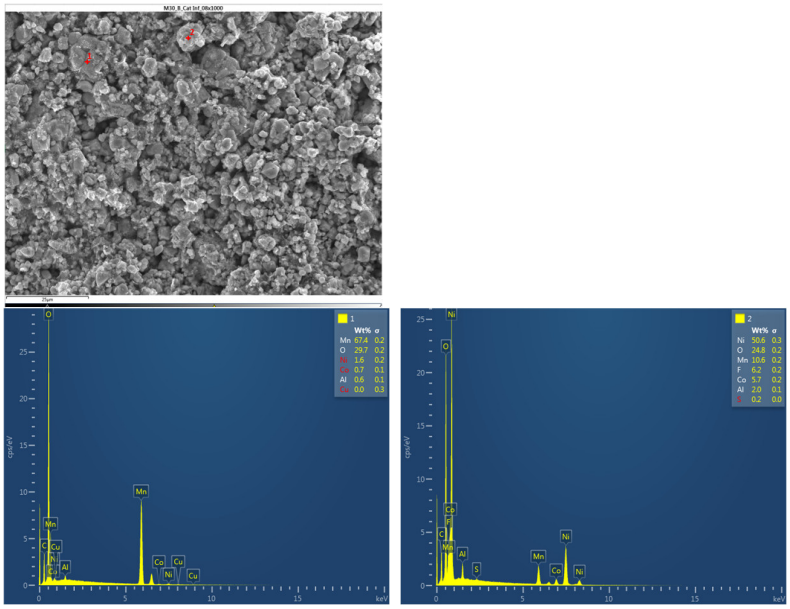

Figure 25. Chemical composition of the lower cathode of module 30.

The distribution of elements in each area of the upper cathode of module 30 is also mapped. This information is also collected with the EDS detector and then processed with the AZtec software.

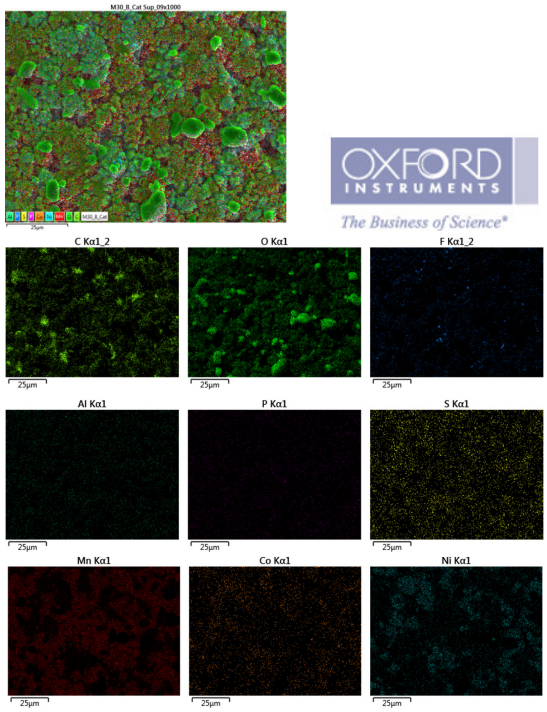

Figure 26. Distribution of elements in each area of the upper cathode of module 30.

Below is a map of the distribution of elements in each area of the lower cathode of module 30.

Preprints (www.preprints.org) | NOT PEER-REVIEWED | Posted: 4 December 2023 doi:10.20944/preprints202312.0101.v1

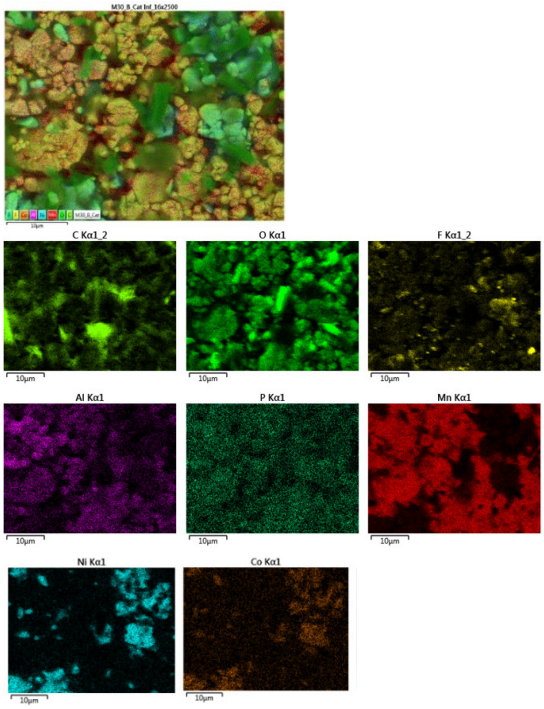

Figure 27. Distribution of elements in each area of the lower cathode of module 30.

In the lower cathode there is a higher amount of fluorine, aluminum, manganese, phosphorus, nickel, and cobalt than in the upper cathode. The following figure shows the chemical composition of the upper cathode of modulo 11. The upper cathode of module 11 also does not show a defined granular surface as in the case of the original cathode, the structure has been broken. The larger particles are about 5 µm in size, so the particles are smaller than in the case of the original cathode. Three different types of structures are observed on the surface of the upper cathode of modulo 11, marked in Figure 28 with three red squares.

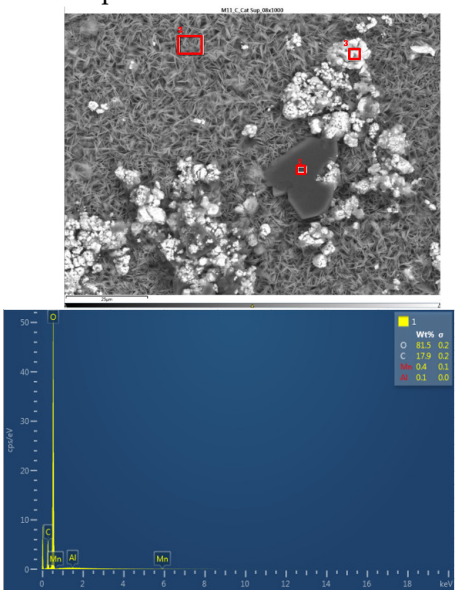

Preprints (www.preprints.org) | NOT PEER-REVIEWED | Posted: 4 December 2023 doi:10.20944/preprints202312.0101.v1

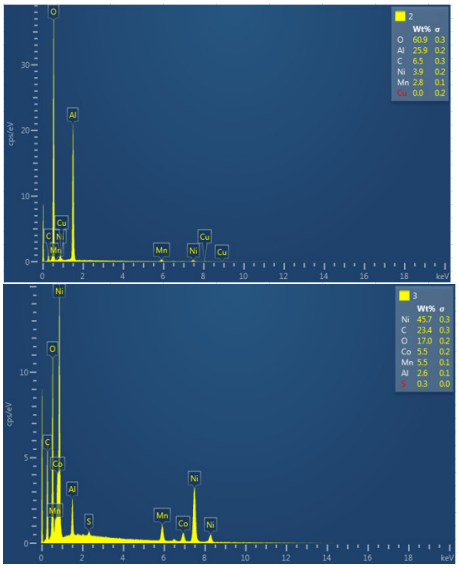

Figure 28. Chemical composition of the upper cathode of module 11.

The results of a detailed analysis of the formed compounds show that the compound marked with "1" had the chemistry of a carbon and oxygen compound, while the second structure was determined to be an aluminum and oxygen compound, formed from the fusion of the cathode aluminum collector, and the third structure was a nickel, carbon, oxygen, cobalt, manganese, and aluminum- containing chemical compound. They are all elements that are products of the cathode and collector coating. Regarding module 11, a higher amount of aluminum is observed, this may be since in this case the aluminum collector has been more damaged than in the case of module 30.

The following figure shows the chemical composition of the lower cathode of module 11. The lower cathode of module 11 also does not show a defined granular surface as in the case of the original cathode, the structure has been broken. Five different types of structures are observed on the surface of the lower cathode of module 11, shown in Figure 29. The results of a detailed analysis of the compounds formed show that the compound marked with "1" had peaks of nickel, manganese, oxygen, copper, carbon, cobalt, and fluorine, so it presents all the elements of the cathode coating, there is also copper that can come from the anode collector. The second structure was a compound of nickel, manganese, cobalt, oxygen, and carbon, and the third structure was compound of copper and oxygen, probably because the anode collector has melted. If compound 4 is analyzed, it is a nickel, oxygen, manganese, and fluoride-containing chemical compound. And finally, compound 5 is a manganese and oxygen compound, formed from the active material of the cathode, and there is also aluminum coming from the aluminum collector of the cathode. In this area appears an aluminum peak this is the result of thermal failure that leaves the aluminum current collector exposed.

Preprints (www.preprints.org) | NOT PEER-REVIEWED | Posted: 4 December 2023 doi:10.20944/preprints202312.0101.v1

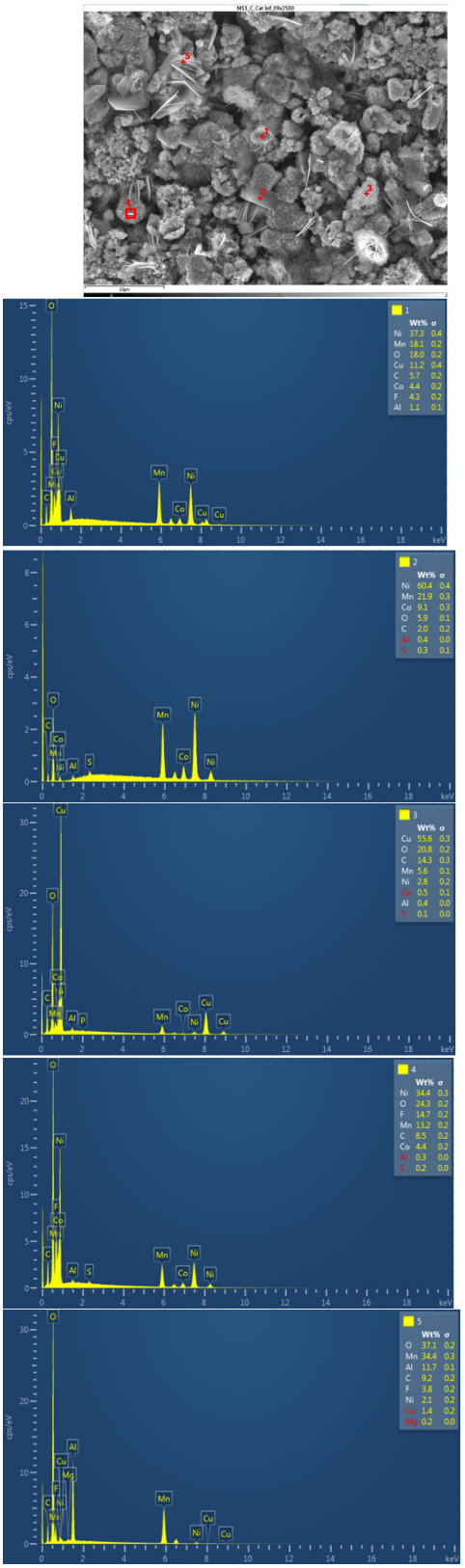

Figure 29. Chemical composition of the lower cathode of module 11.

The following images compare different images obtained with FESEM of the upper anode of module 30, module 11 and the new cell. And in the Figure 31, it is compared different images obtained with FESEM of the lower anode of module 30, module 11 and new cell.

Preprints (www.preprints.org) | NOT PEER-REVIEWED | Posted: 4 December 2023 doi:10.20944/preprints202312.0101.v1

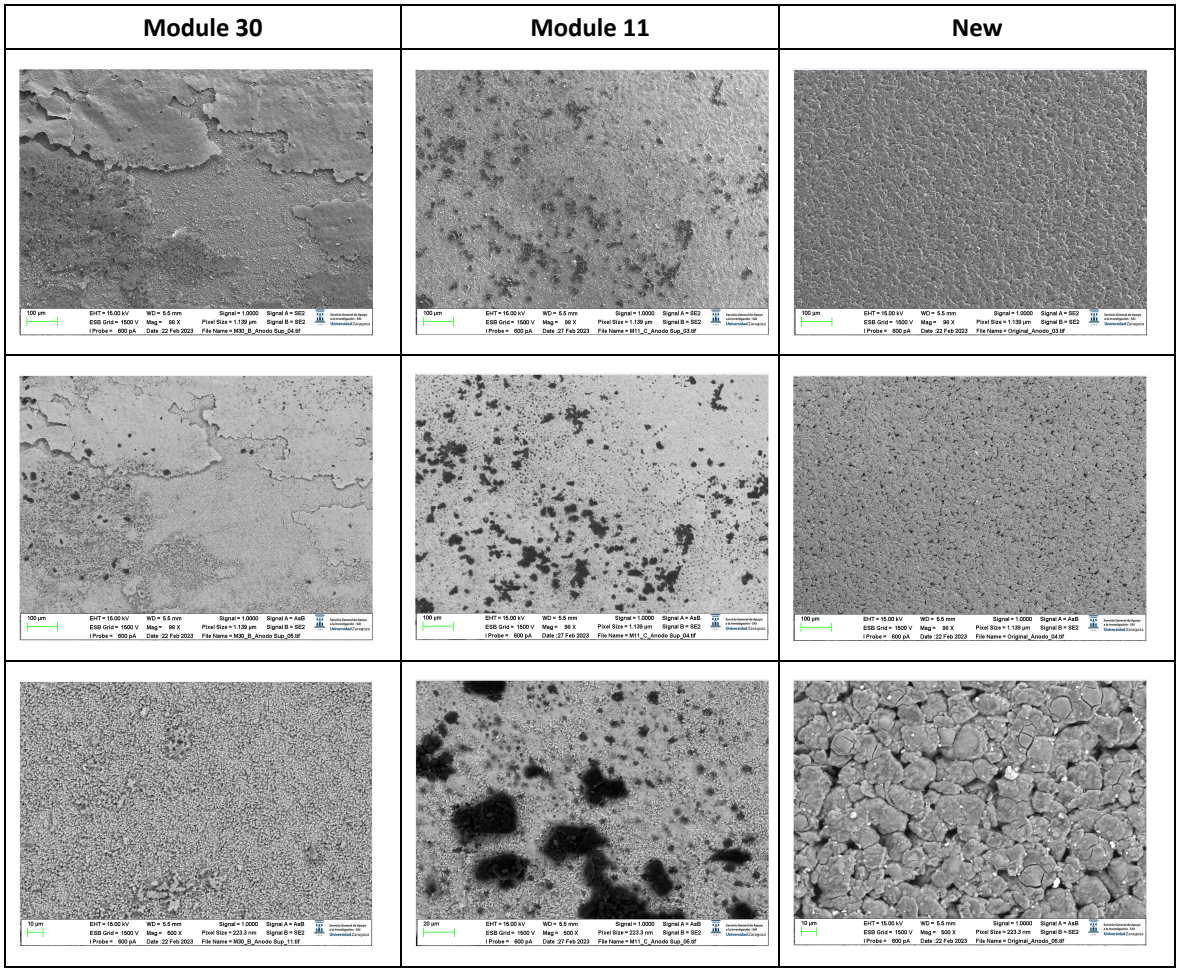

Figure 30. Comparison of images obtained with the FESEM of different areas of the upper anode of module 30, module 11 and the new cell.

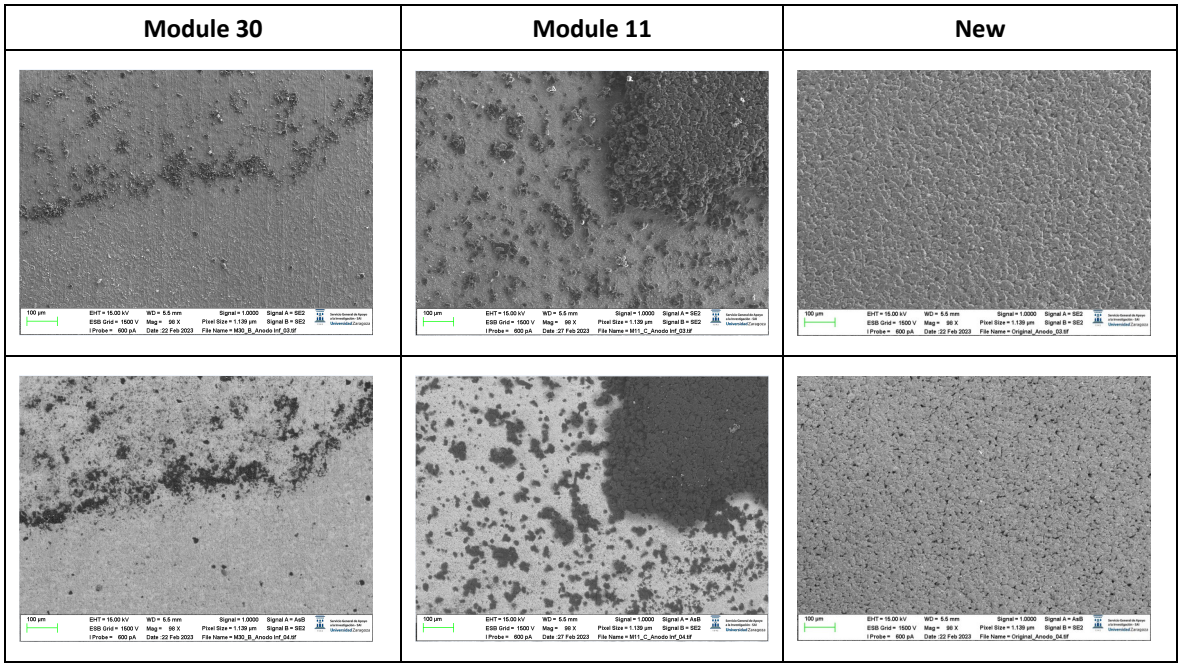

Preprints (www.preprints.org) | NOT PEER-REVIEWED | Posted: 4 December 2023 doi:10.20944/preprints202312.0101.v1

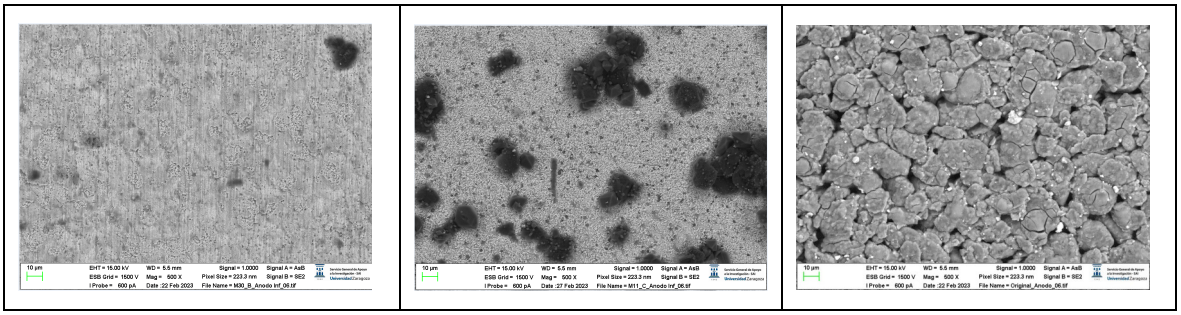

Figure 31. Comparison of images obtained with the FESEM of different areas of the lower node of module 30, module 11 and the new cell.

With respect to the anode electrodes in the previous figure, as it has been done with the cathode electrodes, the anode of an original cell with two anodes (one upper and one lower), it has been compared with module 30 and module 11 of the battery of the burning Nissan Leaf, i.e., after experiencing the Thermal Runaway. It is observed that after experiencing the Thermal Runaway, that spherical particles exist on the surface of the graphite anode. These spherical surfaces are covered with smaller stereoscopic particles as can be seen in Figures 30 and 31.

The original graphite anode has a porous structure that disappears when it undergoes a TR because the pores are occupied by spherical particles. The formation of stereoscopic particles is related to the exothermic reaction on the anode side when TR occurs. On the other hand, at higher temperatures, the intercalated carbon can react with the electrolytes to form Li_2CO_3 [31] since at a temperature above 120 °C the SEI decomposes. In addition, as the temperature increases, at approximately 290 °C, the lithiated carbon could react with fluorine to form LiF [31].

After the analysis of the state of the cathode and anode after experiencing the TR, it is concluded that the spherical structure of the active materials of the cathode and the flake structure of the graphite are destroyed. To obtain the sample from the ignited modules, the cathode and anode were joined together, and it was quite difficult to identify them.

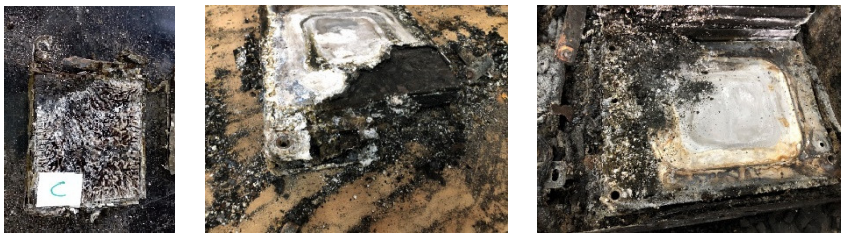

a) b) c)

Figure 32. a. Cell c of module 30, b. Module 11 set on fire, c. Module 30 burned down.

It is observed that there are many impurities on the surface of the electrode. The shape of these impurities is not regular. Sometimes it is rectangular and sometimes it is spherical. The surface distribution is chaotic as can be seen in Figure 32b,c. Because the temperature at which TR is reached in NMC pouch cells is high, the aluminum current collector of the cathode electrode is oxidized and bonded to the anode. Therefore, it is normal to observe debris in the image observed with the SEM. Studies [30] indicate that these debris can be fragments of cathode materials, cathode and separator ash, products of exothermic reactions, as well as graphite flaking. In some areas, a dense and brittle layer has been found on the surface of the electrode. In other areas, flake graphite particles were found under this layer. Thus, it follows that this layer was a completely oxidized aluminum current collector. Unlike in the cathode, the pores of the anode have been clogged by materials from TR reactions. In some areas, a dense, brittle layer covering the surface of the electrode is also observed. In other areas, flake graphite particles were observed under this layer. Therefore, the authors speculated that this layer was a completely oxidized Al current collector. Judging by the structure of the base layer, it was the layer of active material on the anode. Unlike the active material coating of

Preprints (www.preprints.org) | NOT PEER-REVIEWED | Posted: 4 December 2023 doi:10.20944/preprints202312.0101.v1

the cathode of new cells, the pores of the electrode that suffered thermal runaway had been completely clogged by the products of the thermal runaway reactions. The active material of the cathode had completely ceased to function. If the structural transformation (morphology analysis with InLens) of the anode materials after the TR is analyzed (Figures 33 and 34) it is observed that in the case of modules 30 and 11 with a SoC of 68% after the TR, the layered structure of the material was destroyed, the particles dispersed outside the original layered structure and adhesion occurred. The positive electrode material (cathode) reacted at high temperature and decomposed. On the other hand, carbon particles from the negative electrode (anode) were get into the positive electrode (cathode) structure through the damaged diaphragm.

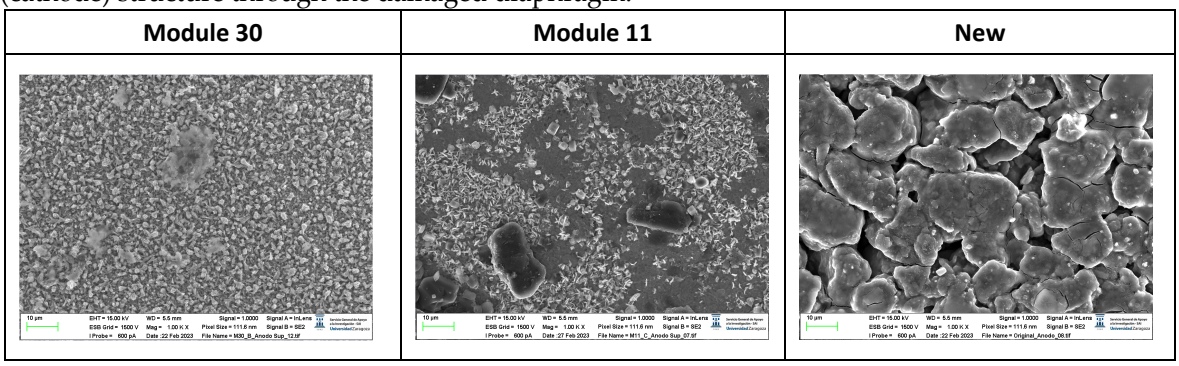

Figure 33. Morphological analysis of the transformation of the upper anode of module 30 and module 11 after the Thermal Runaway compared with the initial anode structure of a new cell.

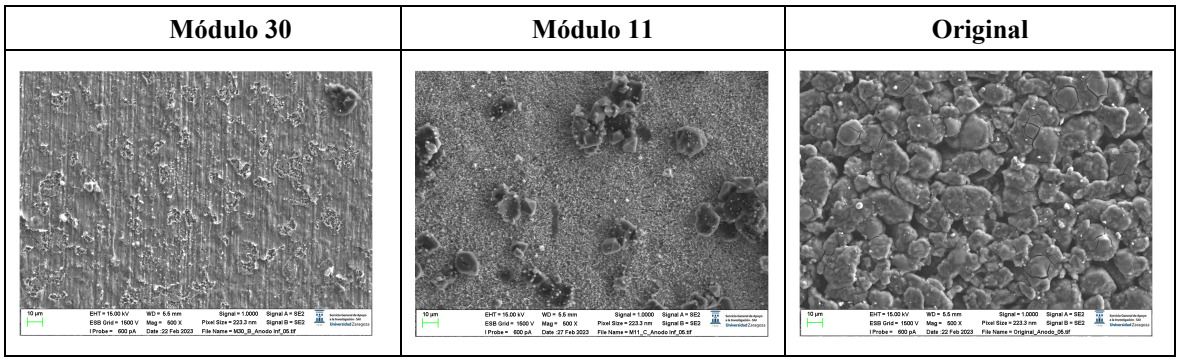

Figure 34. Morphological analysis of the transformation of the lower anode of module 30 and module 11 after the Thermal Runaway compared with the initial anode structure of a new cell.

The chemical composition of the new cell anode is then analyzed. The anode has a granular structure. The diameter of the largest particles was 14 μm. Four types of structures are identified. The results of the chemical analysis revealed a high content in zone 2 of carbon (C), which allows the active material of the anode to be identified as graphite. There are traces of phosphorus (P) that can be identified as remnants of the electrolyte (assumed to be LiPF6 dissolved in a carbonate mixture solvent). Also, in zone 1 a fluorine peak is identified, it can be seen on the surface of the graphite particles and can be attributed to the decomposition of the electrolyte that is part of the SEI. The small peaks of Cu can be attributed to the preparation of the sample and can be neglected. On the other hand, in zones three and four, peaks of calcium and iron are identified, due to the shape of which impurities can be considered that have appeared due to the preparation of the sample. Manganese also appears.

Preprints (www.preprints.org) | NOT PEER-REVIEWED | Posted: 4 December 2023 doi:10.20944/preprints202312.0101.v1

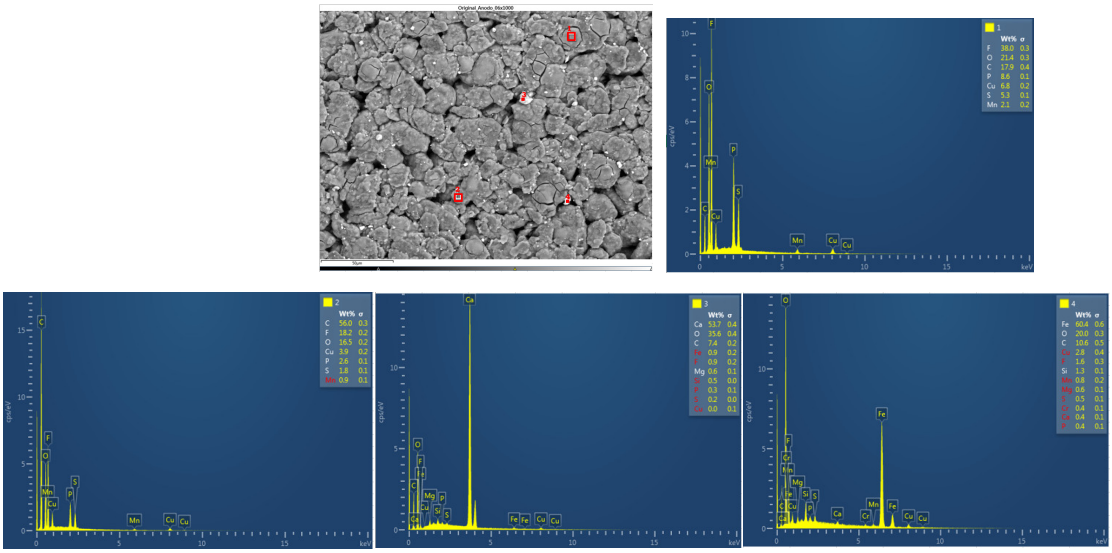

Figure 35. Chemical composition of the new cell anode.

The following figure shows the chemical composition of other structures identified in the original anode. Structure 1 identifies a chemical compound of manganese and oxygen, and structure 2 identifies a chemical compound of carbon and oxygen with fluorine, which may be due to electrolyte, copper, phosphorus, and sulfur (the latter three elements may be due to impurities from sample preparation).

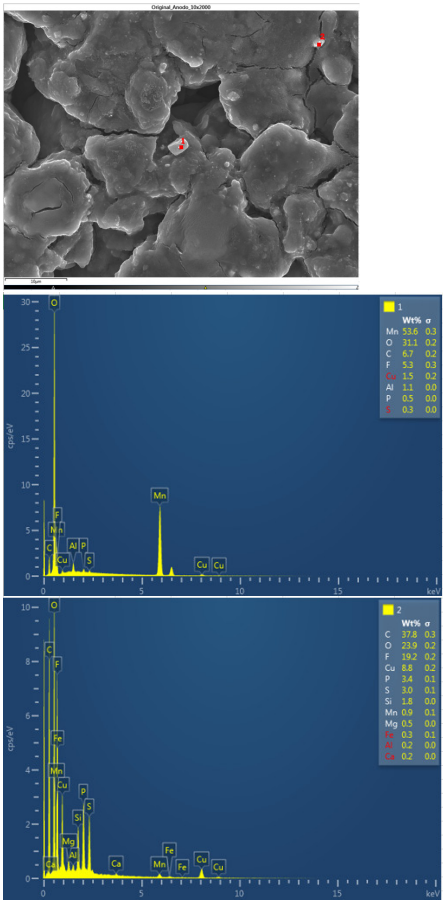

Figure 36. Chemical composition of the new cell anode 2.

Preprints (www.preprints.org) | NOT PEER-REVIEWED | Posted: 4 December 2023 doi:10.20944/preprints202312.0101.v1

Afterwards, the chemical composition of the upper anode of the ignited module 30 is analyzed. The upper anode of module 30 also does not show a defined granular surface as in the case of the original anode, the structure has been broken. Three different types of structures were observed on the surface of the upper anode of module 30, shown in Figure 37. The results of a detailed analysis of the compounds formed show that the compound marked with "1" had the chemical of a copper and oxygen compound, which may be due to the anode collector having melted due to the elevated temperatures, and the second structure was also identified as a copper and oxygen compound, while structure 3 was a carbon and oxygen compound, it may be due to the coating of the graphite anode.

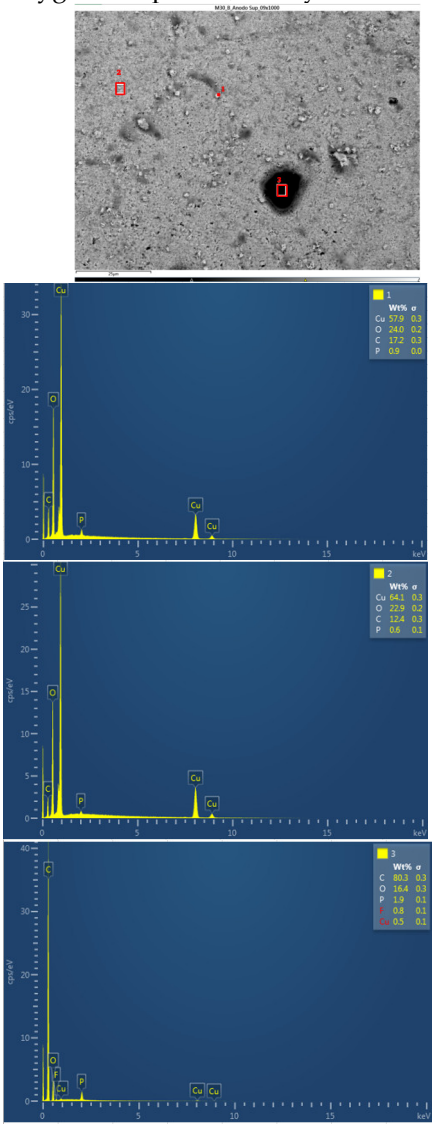

Figure 37. Chemical composition of the upper anode of module 30.

In Figure 38 below, the chemical composition in another area of the upper anode of the ignited module 30 is analyzed. Five different types of structures were observed on the surface of the upper anode of module 30. All five structures feature copper, carbon, and oxygen.

Preprints (www.preprints.org) | NOT PEER-REVIEWED | Posted: 4 December 2023 doi:10.20944/preprints202312.0101.v1

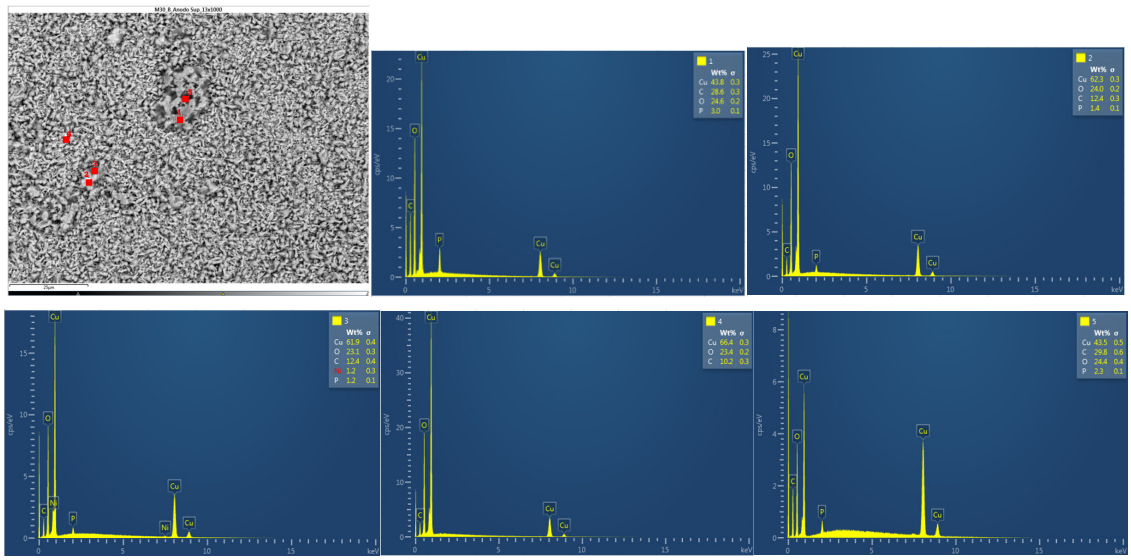

Figure 38. Chemical composition of the upper anode of module 30.

In Figure 39 below, the chemical composition in another area of the upper anode of the ignited module 30 is analyzed. Four different types of structures were observed. In the first three ones a compound of copper, carbon and oxygen was observed. In zone 4, fluoride, copper and oxygen were identified, the existence of fluoride is due to the electrolyte and the existence of copper is due to copper from the anode collector.

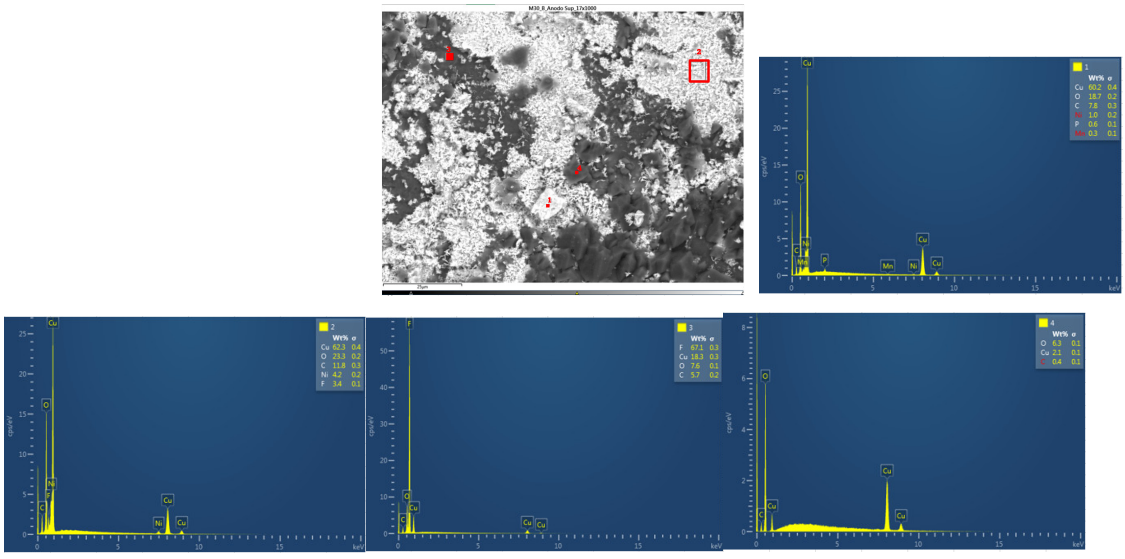

Figure 39. Chemical composition of the upper anode of module 30.

Next, the chemical composition of the lower anode of the ignited module 30 is analyzed. The lower anode of module 30 also does not show a defined granular surface as in the case of the original anode, the structure has been broken. Two different types of structures were observed on the surface of the lower anode of module 30, shown in Figure 40. The results of a detailed analysis of the compounds formed show that the compound marked with "1" had the chemistry of a Carbon and oxygen compound, which may be due to the anode coating, and the second structure features copper, carbon, and oxygen.

Preprints (www.preprints.org) | NOT PEER-REVIEWED | Posted: 4 December 2023 doi:10.20944/preprints202312.0101.v1

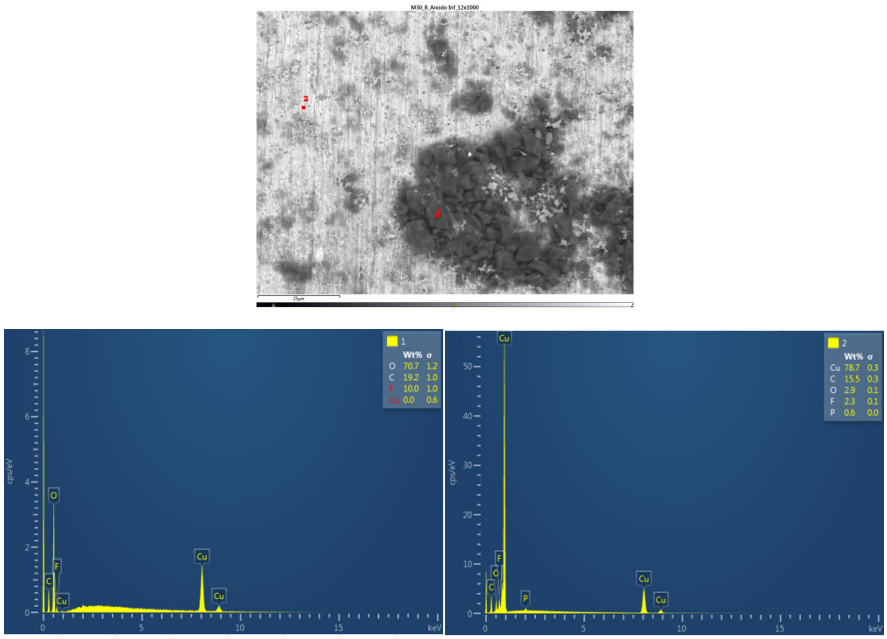

Figure 40. Chemical composition of the lower anode of module 30.

Figure 41 below shows the chemical composition in another area of the upper anode of the ignited module 11. Six different types of structures were observed on the surface of the upper anode of module 11. The first structure is carbon, coming from the graphite of the anode coating, the second structure was a compound of fluorine, copper and oxygen, fluorine comes from the electrolyte, the rest of the structures have copper, carbon, and oxygen.

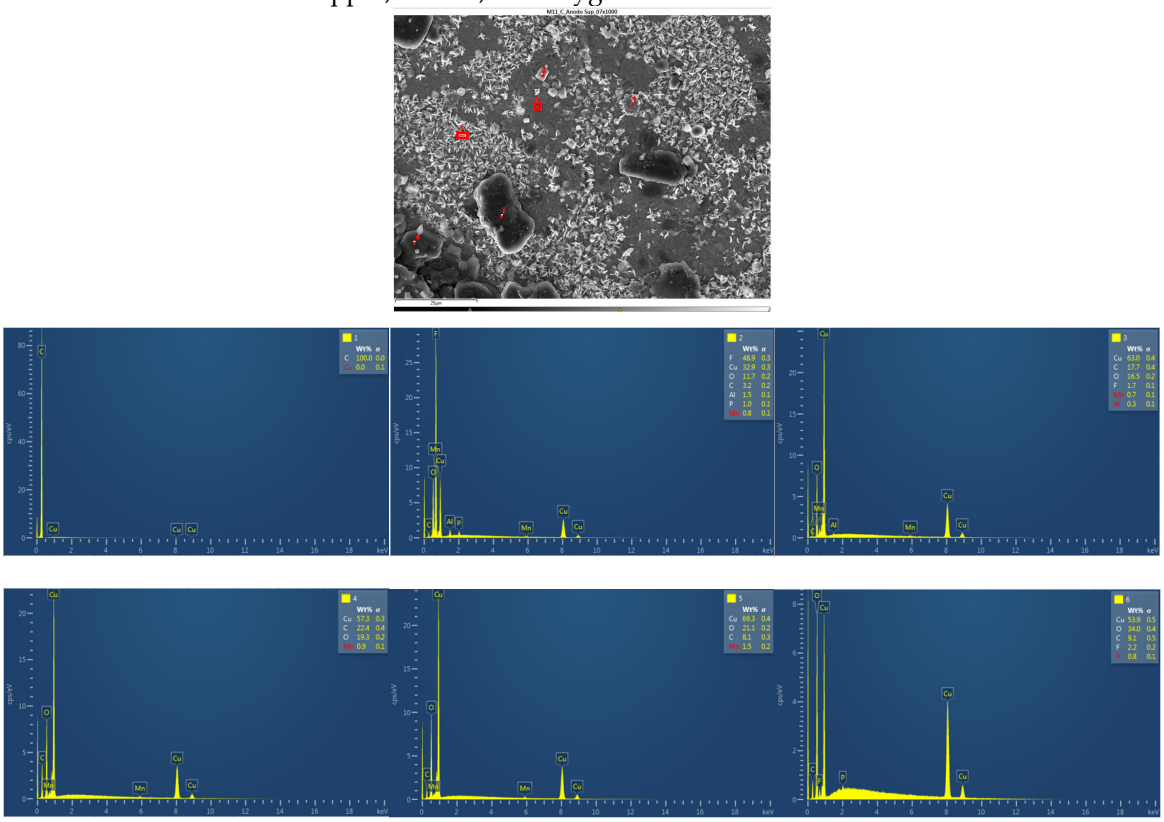

Figure 41. Chemical composition of the upper anode of module 11.

And finally, in the following figure 42, the chemical composition in another area of the lower anode of the burning module 11 is analyzed. Six different types of structures were observed on the

Preprints (www.preprints.org) | NOT PEER-REVIEWED | Posted: 4 December 2023 doi:10.20944/preprints202312.0101.v1

surface of the lower anode of module 11. The first structure was a compound of fluorine, copper, and oxygen, in structure 2 was identified copper and oxygen, structure 3 is like the first, a compound of fluorine, copper and oxygen. In structure 4 there is more copper than fluorine and oxygen, and in structures 5 and 6, there is copper oxide and carbon oxide.

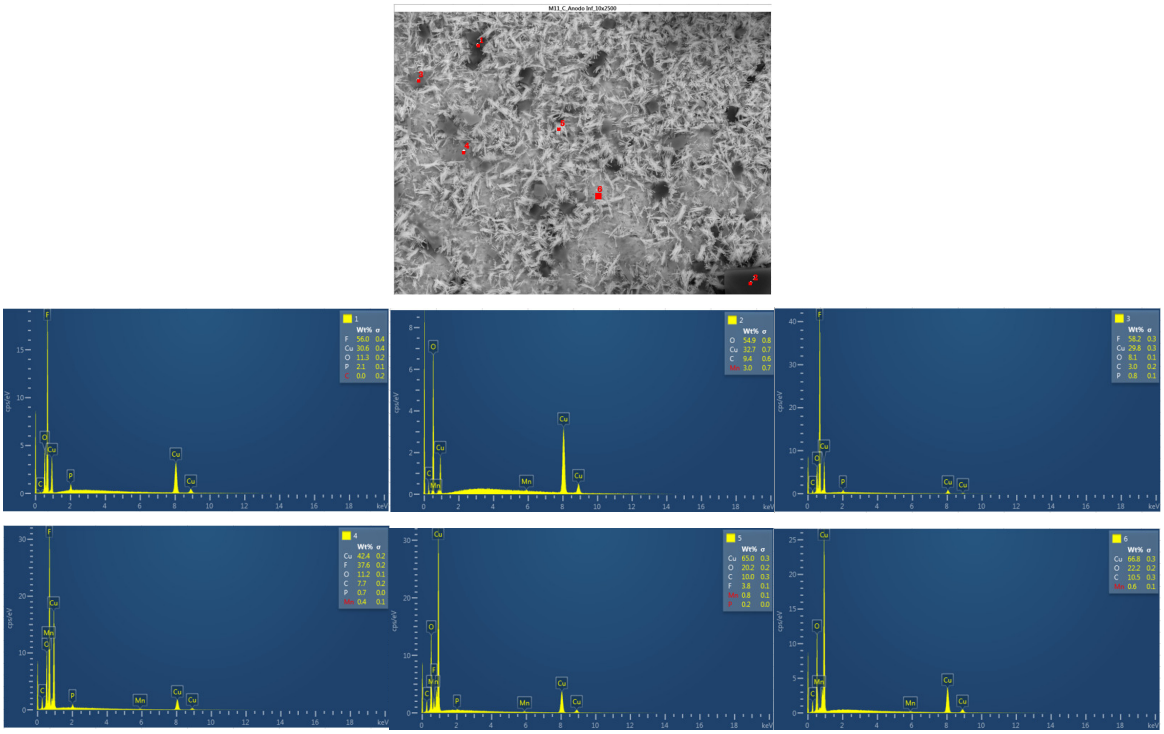

Figure 42. Chemical composition of the lower anode of module 11.

The analysis of the cell anodes after the fire test, shows that the anode has peaks of oxygen and peaks of carbon, which indicates the formation of lithium carbonate (Li_2CO_3).

A morphological analysis of the separator of the new cell is then performed since the separator cannot be recovered in the burned modules because it has melted in the thermal runaway reaction. The surface structure of the separator was investigated to determine the thickness of the separator fibers and the size of the pores, as well as to determine whether an alumina layer had been deposited on the separator membrane, as indicated above. Figure 43 shows the results of the SEM image. On the right is shown the structure of the fibers of the polypropylene membrane, (C3H6)n. The separator fibers were aligned in a direction perpendicular to the cell tabs.

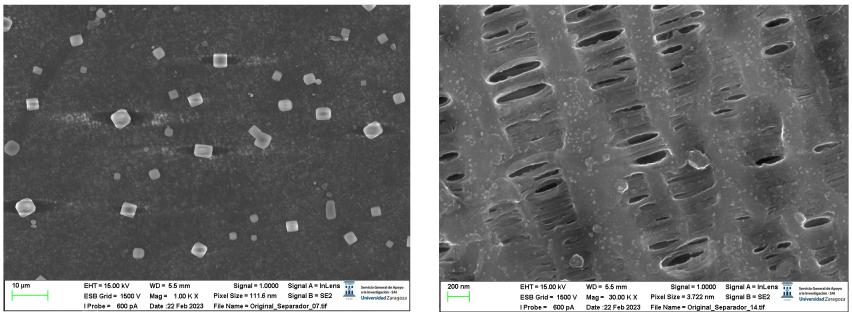

Figure 43. Morphological analysis of the separator.

The total thickness of the separating fiber was about 289 nm, as shown in Figure 44. The analyzed structure shows pores of different diameters, the smallest of about 41.61 nm and the largest about 88.78 nm. A general requirement for pore size in lithium-ion cells is that they must be in the submicron range to prevent dendritic penetration of lithium from occurring over the life of the battery [37].

Preprints (www.preprints.org) | NOT PEER-REVIEWED | Posted: 4 December 2023 doi:10.20944/preprints202312.0101.v1

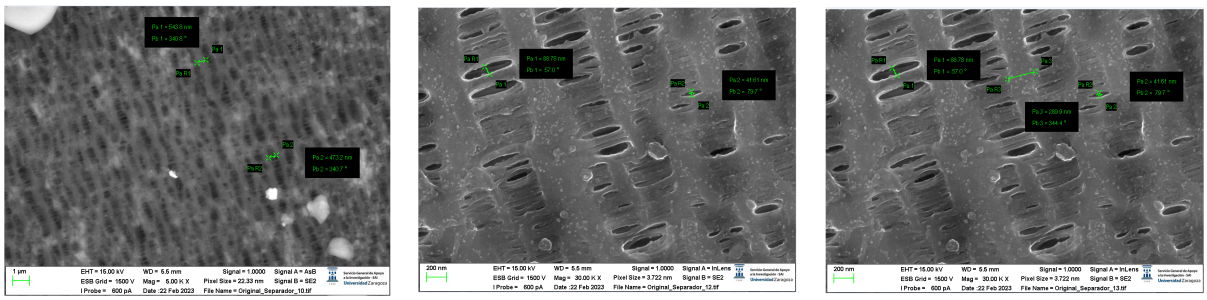

Figure 44. Morphological analysis of the separator. Measurement.

After that, the analysis of the chemical composition of the separator will be performed. There are three types of structures, the first being carbon with fluorine and phosphorus. The carbon is from the structure of the polypropylene separator itself; the fluorine comes from the electrolyte with which it is soaked, and the phosphorus may be due to an impurity in the preparation of the sample. Structure 2 and 3 have the same composition as the first structure.

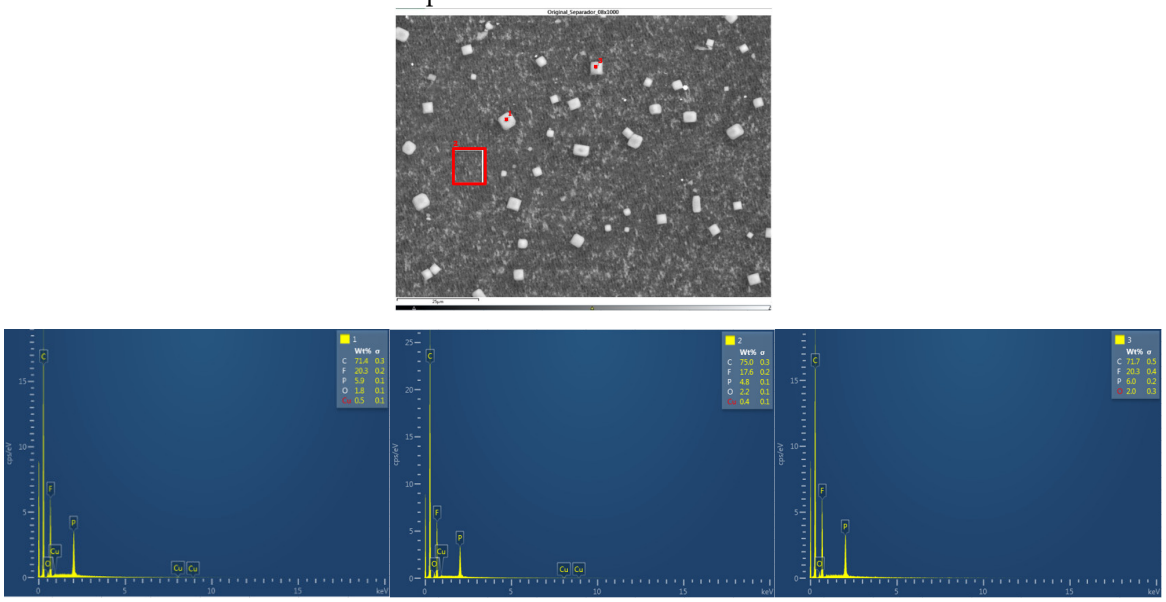

Figure 45. Chemical composition of the separator.

The layered structure was destroyed when the thermal runaway occurred. In the battery sample with 68% SoC, there were characteristic fluoride peaks, indicating that the cathode material reacts with the electrolyte after decomposition [38]. Characteristic carbon peaks are also shown, this is because, in the Thermal Runaway reaction, some of the carbon dust was get into the positive electrode material through the broken diaphragm [39]. It is observed that in the samples of module 11 and module 30, in which a Thermal Runaway reaction has occurred, the structure of the positive electrode (anode) sample is destroyed, and the particles were dispersed outside the original stratified structure, and the adhesion phenomenon occurred, showing fragmentation. Particles cannot be found, and external impurities are placed inside the structure [40].

The battery that caught fire in the test had 68% SoC. There are studies [36] that indicate that in the case of NMC batteries the increase in SoC makes the thermal runaway reaction more intense, the temperature at which the thermal runaway starts is reduced, and the structural damage to the electrode materials is strong. In high-temperature conditions, the internal diaphragm of the battery has been destroyed, which will cause a short circuit inside the battery and aggravate the thermal runaway reaction. The structure of the positive electrode material is destroyed in the thermal runaway reaction, and the particles are exposed and dispersed outside the structure and adhered to the negative electrode.

Preprints (www.preprints.org) | NOT PEER-REVIEWED | Posted: 4 December 2023 doi:10.20944/preprints202312.0101.v1

If the particle size distribution (PSD) is compared for the case of the new cell and the burnt cells, it is observed that in the case of the latter, the particles of the aluminum negative cathode are smaller, they are further apart to facilitate the passage of gases and this gap will be occupied by another particle. In the case of burning cells, the particles are much smaller than in the case of new cells. Heat generation depends on the surface area and particle size of the positive electrode or cathode. There are studies [41] that show that the microstructure of particles can influence exothermic reactions of exothermic degradation.

3.3.2. Structural Tests Resulst: Layer properties of the cell and identification of cell details

In this section, the transversal-section investigation of the cells will be carried out, which will allow obtaining information about the structure and manufacture of the cells, and the thickness measurement of each of the layers of the cell will be carried out.

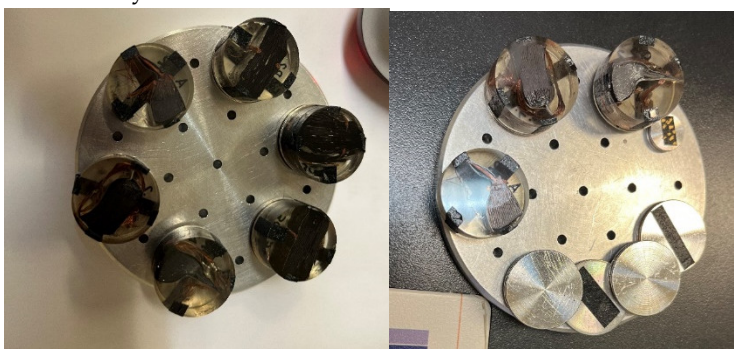

Figure 46. Preparation of samples from the section of cells to be analyzed under the microscope, embedded in resin, and polished.

The stacking of the different layers of the cell will be analyzed in transversal-section, which will allow to identify interesting manufacturing details of the pouch cells. First, the sample taken from zone 3 is analyzed, the central area on the opposite side to the side where the battery tabs of the cell are.

It is observed that all the separating membranes are welded to the bag at the sealing point near the edge. Regarding the mechanical behavior of the cell and possible failure of it, this fact indicates that the separator could experience high tensile strain if a mechanical force acted on the battery near this axis and mechanical rupture of the separator membrane could occur. This would cause the battery electrodes to come into contact, which is the prerequisite for experiencing an electrical failure and thermal runaway. It is observed that near the edge of the battery the distances between layers are smaller due to the hot-soldered area of the bag. The lack of layers on this section of the battery ensures that no short circuits will occur, even if some of the battery layers were to get too close to each other.

Another purpose of an anode layer that is longer than the cathode is to increase the rigidity of the battery near the edge, which smooths the distribution of charge in the event of charging at the edge. The investigated cell contained 18 anodic layers, 17 cathode layers, and 34 separator sheets. The electrodes on both sides of the battery were anodes. This observation suggests that the active material deposited on the outer face of the last copper foil remained electrochemically inactive and did not participate in the charge transfer or energy storage process.

In lithium-ion batteries, a layer of aluminum oxide (Al_2O_3) is usually deposited on the separator membrane to improve its thermal resistance, also improving its thermal properties.

Preprints (www.preprints.org) | NOT PEER-REVIEWED | Posted: 4 December 2023 doi:10.20944/preprints202312.0101.v1

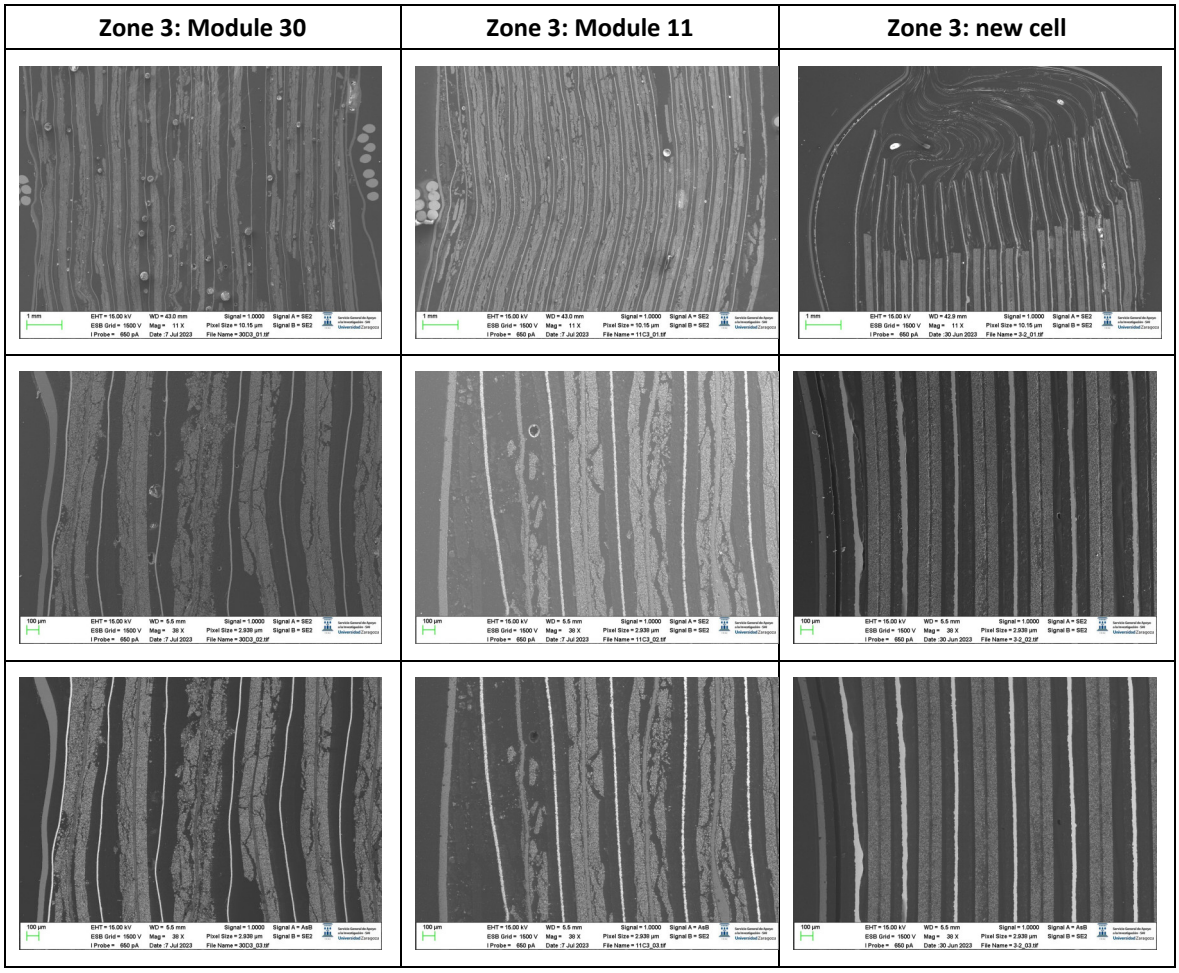

Figure 47. Images of the section of the pouch cell in zone 3 (central area of the opposite side to the one where the battery tabs of the cell are located).

If the morphology is analyzed, it can be concluded that the outer area of zone three is more damaged in the case of module 11, while in the case of module 30 the central area is more damaged. It is also observed that the thickness of the copper collector decreases in case of thermal runaway, and it is observed to be narrower for module 30. To know the chemical composition of zone 3 in the original cell, a map of the distribution of elements was made. The copper collector (yellow) and the aluminum collector (blue) are identified. The coating of the anode is also observed, which is made of graphite (carbon, red color) and the coating of the cathode (composed of oxygen, manganese, nickel). Electrolyte fluoride is also observed.

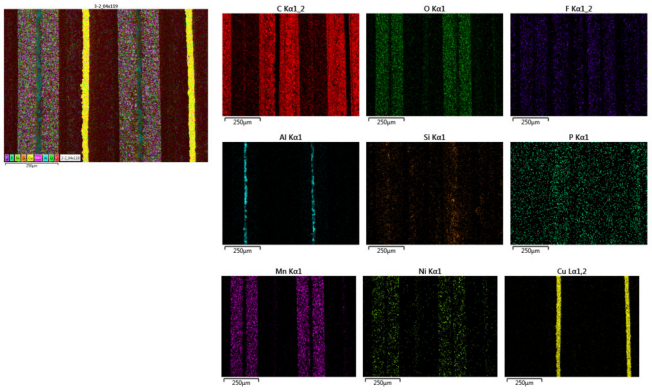

Figure 48. Distribution of the elements of a new pouch cell in zone 3 (central area of the opposite side to the one where the battery tabs of the cell are located).

 doi:10.20944/preprints202312.0101.v1

After that, the chemical composition of zone 3 was analyzed for the case of the cell of the burned module 30.

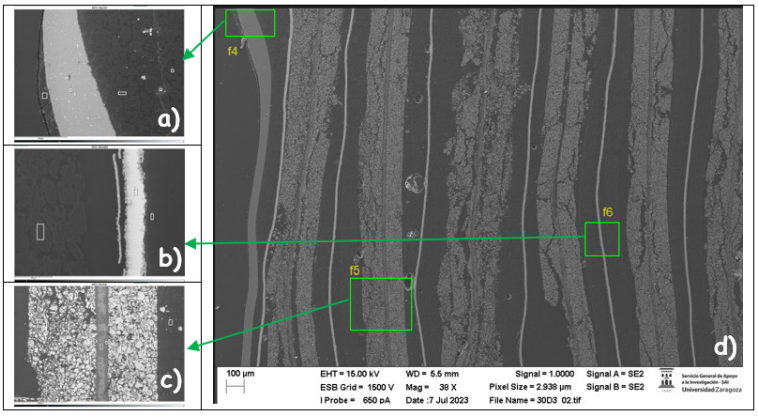

Figure 49. Chemical composition of each of the layers of the pouch cell of module 30 in zone 3 (central zone of the opposite side to that of the battery tabs of the cell).

Figure 49.a identifies the pouch of the pouch cell which is made of aluminum (zones 2 and 3). In zone 5 there is carbon that may be graphite from the anode coating. Figure 49.c identifies the cathode (manganese nickel oxide) and there are also carbon particles. Around the aluminum manifold, alumina (Al_2O_3) has been deposited on the separator in the cathode area. Alumina (aluminum oxide) has been deposited. In Figure 49.b the anode area has been detected, graphite (carbon) coating, then there is a layer with cooper and oxygen and the anode collector shell.

Moreover, the chemical composition of zone 3 is analyzed in the case of the cell of the burning module 11.

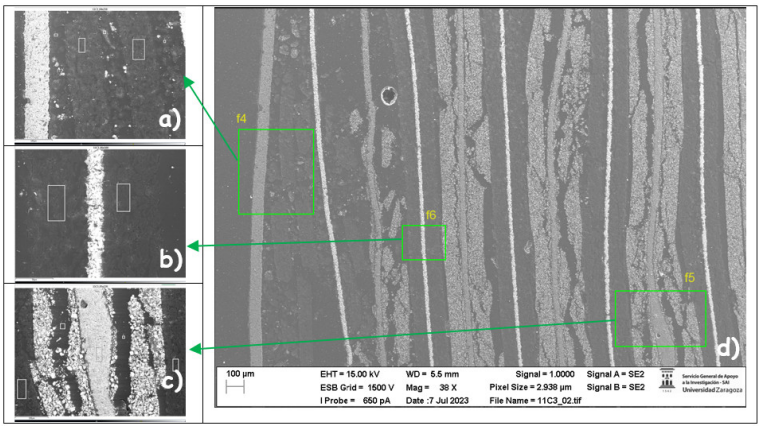

Figure 50. Chemical composition of each of the layers of the pouch cell of module 30 in zone 3 (central zone of the opposite side to that of the battery tabs of the cell).

Figure 50.a identifies the pouch of the pouch cell which is made of aluminum (zone 1 and 2), it appears more damaged than the bag of module 30. In zones 6 and 8 there is compound of carbon and oxygen with some fluorine from the electrolyte and in zone 7 there is a compound of carbon and oxygen with aluminum from the cathode collector. Figure 50.c identifies the cathode (manganese oxide) and there are also carbon particles. In this case, aluminum is not observed. In Figure 50.b the anode zone has been detected, then there is a copper layer, copper collector and then there are silicon particles and then a graphite coating layer is detected. The silicon particles could be due to traces of a sealant material.

The sample obtained in zone 1 (anode battery tabs) is analyzed below:

Preprints (www.preprints.org) | NOT PEER-REVIEWED | Posted: 4 December 2023 doi:10.20944/preprints202312.0101.v1

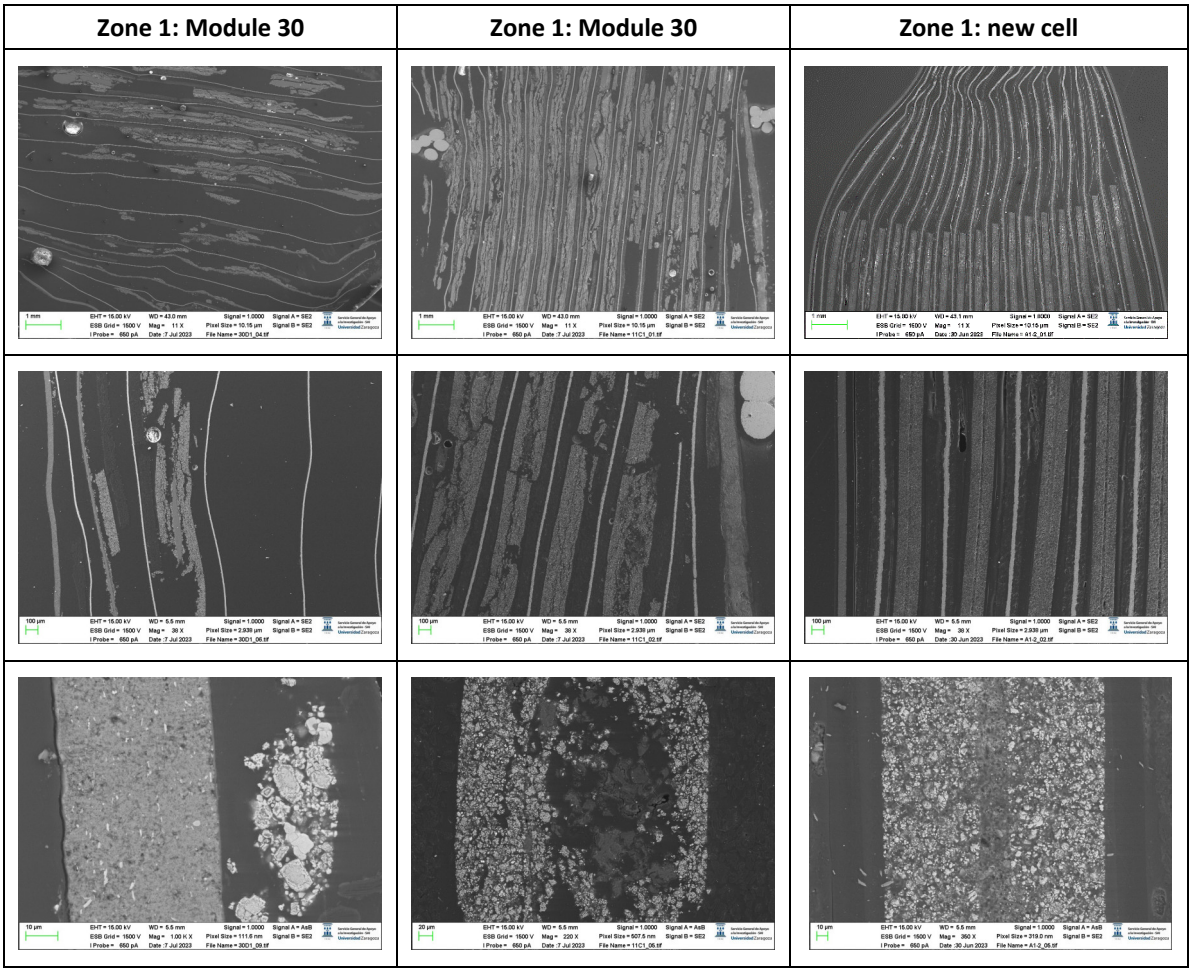

Figure 51. Images of the pouch cell section in zone one (anode zone) of the cell.

If the morphology is analyzed, it can be observed that in zone one module 30 is more damaged than module 11. It is also observed that the thickness of the copper collector decreases in the case of thermal runaway, and it is observed to be narrower in the case of module 30.

Subsequently, the chemical composition of zone 1 is analyzed in the case of the cell of module 30 that caught fire.

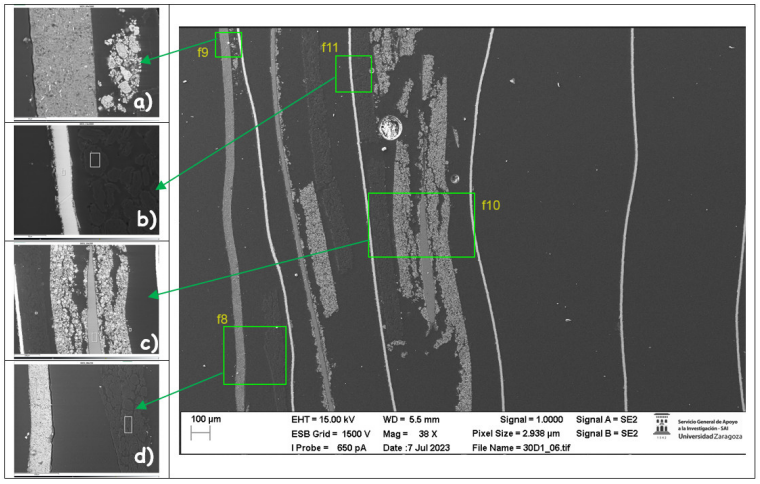

Figure 52. Chemical composition of each of the layers of the pouch cell of module 30 in zone 1 (anode zone).

Figure 52a identifies a compound of nickel and oxygen in zone 1 with traces of carbon and manganese, a compound of manganese and oxygen in zone 2 and a compound of carbon and oxygen

Preprints (www.preprints.org) | NOT PEER-REVIEWED | Posted: 4 December 2023 doi:10.20944/preprints202312.0101.v1

in zone 3. Figure 52.b identifies a compound of copper, carbon, and oxygen in zone 1 and zone 3, copper in zone 2 which is the anode collector, and a compound of carbon and oxygen in zone 4. Figure 52.c identifies carbon, anode coating in zone 1, a compound of manganese, oxygen, and carbon in zone 2, cathode coating in zone 2, cathode aluminum collector in zone 3, fluorine from the electrolyte in zone 4, and a compound of aluminum and oxygen in zone 5. Finally, Figure 52.d identifies a compound of copper, carbon, and oxygen in zones 1 and 3, copper in zone 2 which is the copper collector of the anode, and a compound of carbon and oxygen in zone 4.

Next, the chemical composition of zone 1 is analyzed in the case of the cell of the burned module 11.

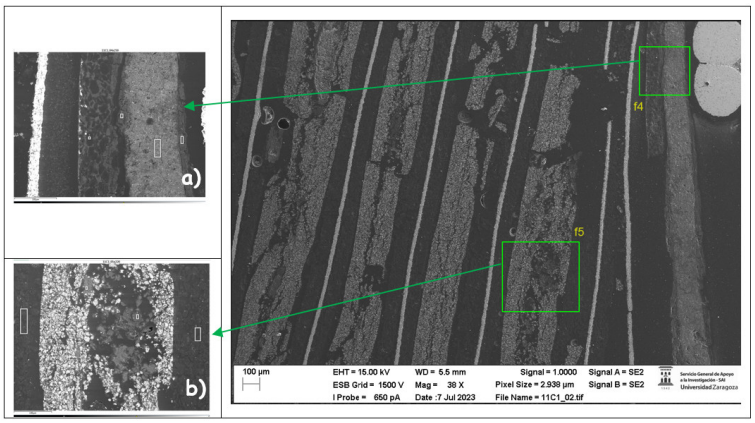

Figure 53. Chemical composition of each of the layers of the pouch cell of module 11 in zone 1 (anode zone).

Figure 53.a identifies a compound of carbon, oxygen, and aluminum in zone 1 and 2, aluminum and carbon in zone 3 which is the pouch bag, in zone 4 carbon, oxygen and aluminum and some copper. And in zone 5 carbon which is the coating of the anode. In Figure 53. B a compound of carbon and oxygen is identified in zone 1, 4 and 5, in zone 4 there is also some aluminum. In zone 2, there is a compound of manganese, carbon and oxygen, cathode coating and in the center, zone 3, there is a compound of aluminum and oxygen from the aluminum collector that has melted down and disappeared.

The chemical composition of zone 1 is then analyzed in the case of the new cell:

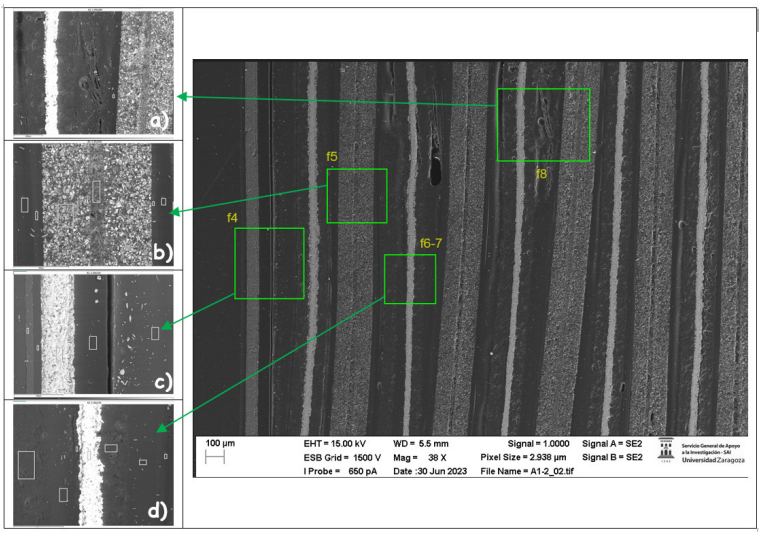

Figure 54. Chemical composition of each of the layers of the new pouch cell in zone 1 (anode zone).

Figure 54.a identifies a compound of carbon and oxygen in the three zones analyzed, Figure 54.b identifies a compound of carbon and oxygen in zones 1, 2, 5 and 6 and a compound of manganese,

Preprints (www.preprints.org) | NOT PEER-REVIEWED | Posted: 4 December 2023 doi:10.20944/preprints202312.0101.v1

carbon, oxygen, and fluoride in zone 3, and carbon and aluminum in zone 4. Figure 54.c identifies the bag that is aluminum in zone 3, coated on both sides by a compound of carbon and oxygen. Figure 54.d identifies the copper collector of the anode in zone 4, which is coated by a compound of carbon and oxygen.

The sample obtained in zone 2 (cathode battery tabs) is analyzed below:

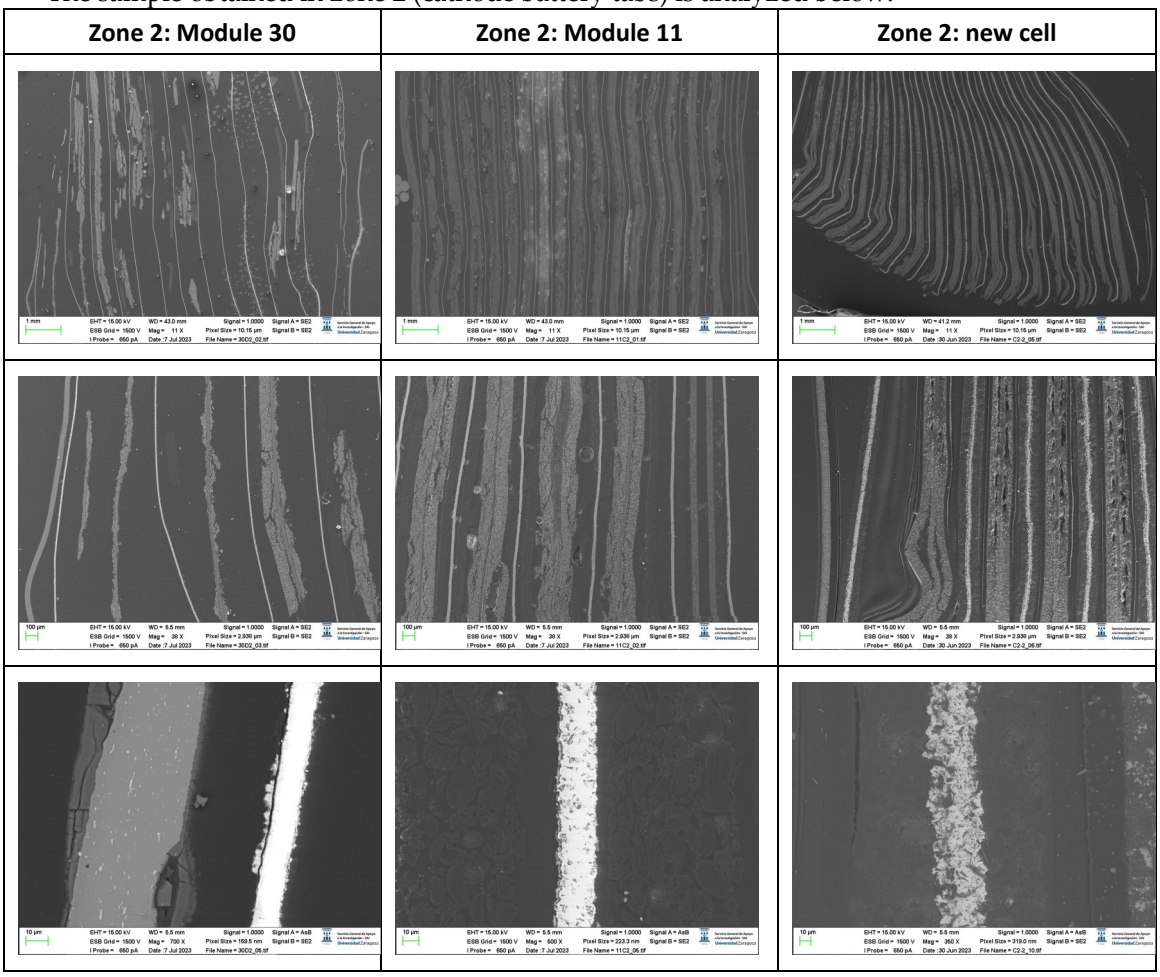

Figure 55. Images of the pouch cell section in zone two (cathode zone) of the cell.

If the morphology is analyzed, in zone 2 module 30 is more damaged than module 11. It is also observed that the thickness of the copper collector decreases in the case of thermal runaway and is observed to be narrower in the case of module 30.

Next, the chemical composition of zone 2 is analyzed in the case of the cell of the burning module 30.

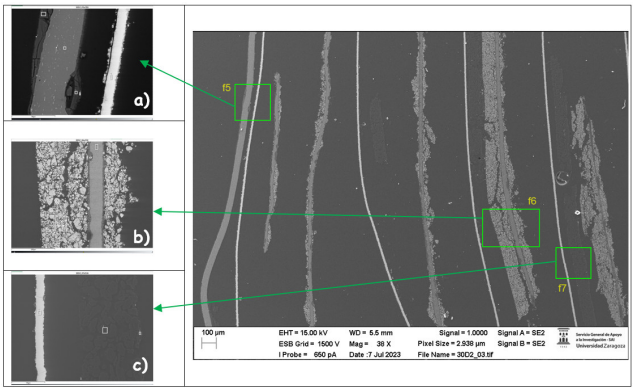

Figure 56. Chemical composition of each of the layers of the module 30 pouch cell in zone 2 (cathode zone).

Preprints (www.preprints.org) | NOT PEER-REVIEWED | Posted: 4 December 2023 doi:10.20944/preprints202312.0101.v1

Figure 56.a identifies a layer of a compound of carbon and oxygen (zone 1), a layer of a compound of aluminum and oxygen (zone 2) and the aluminum pouch (zone 3), a layer of an aluminum and oxygen compound (zone 5) and a layer of a carbon and oxygen compound (zone 6), anode copper collector (zone 8), and a layer of a compound of cooper and oxygen (zone 7 and zone 9). Figure 56.b identifies a compound of manganese, carbon, and oxygen in zone 1 and 5, a layer of an aluminum and oxygen compound in zones 2 and 4, and aluminum and carbon in zone 3, the cathode collector. Figure 56.c identifies a compound of copper, carbon, and oxygen in zones 1 and 3 and copper and carbon in zone 2, which is the collector and anode.

Next, the chemical composition of zone 2 is analyzed in the case of the cell of the burning module 11.

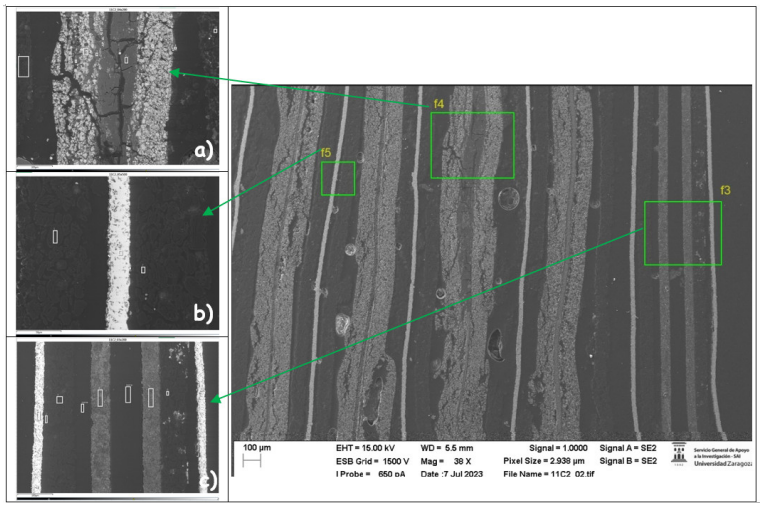

Figure 57. Chemical composition of each of the layers of the module 11 pouch cell in zone 2 (cathode zone).

Figure 57.a shows the cracking of the collector and cathode coating, identifying a compound of aluminum and oxygen (zone 2 and zone 4) within a layer of manganese, carbon, nickel, and oxygen (zone 3). Figure 57.b identifies a layer of carbon (zone 1 and zone 7), a layer with a compound of copper, carbon, and oxygen (zone 2, 3), a zone with a compound of copper and oxygen, that is the collector of the anode, and a zone that has silicon (zone 5 and zone 6). Figure 57.c shows a copper zone (zone 1 and zone 8) with two collectors, zones 4 and 5 are carbon and aluminum, resin layers are also identified and in zone 7 carbon with traces of silicon and copper is observed. The silicon particles could be due to traces of a sealant material.

The chemical composition of zone 2 is then analyzed in the case of the new cell.

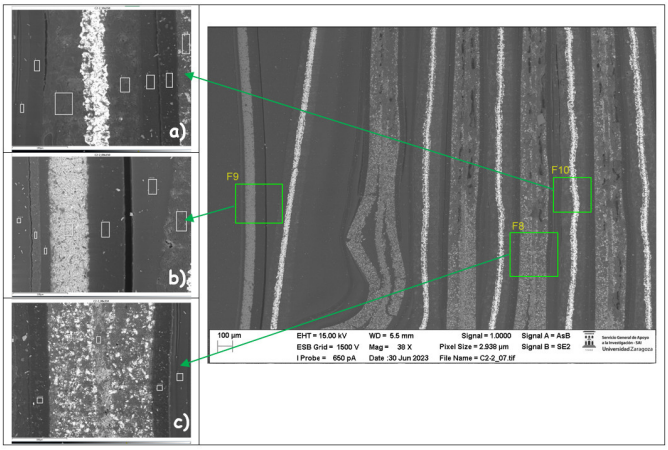

Figure 58. Chemical composition of each of the layers of the new pouch cell in zone 2 (cathode zone).

 doi:10.20944/preprints202312.0101.v1

Figure 58.a shows the copper collector with carbon and some silicon (zone 4), a layer of a compound of carbon and oxygen on either side of the collector that comes from the graphite in the anode. Figure 58.b shows the aluminum pouch with carbon and a compound of carbon and oxygen layers. Figure 58.c shows layers of a carbon and oxygen compound, zone 3 shows aluminum and carbon, zone 4 shows a compound of manganese and oxygen, and zone 5 shows carbon and silicon. As stated above the silicon particles could be due to traces of a sealant material.

5. Conclusions

After analyzing the results obtained on the state of the cells subjected to thermal runaway in each of the analyzed arrangements, both vertical and horizontal arrangement, and compared with the state of a new cell, the following conclusions are reached:

- After thermal runaway the cathode surface is covered with off-white floccules, fragment debris from cathode materials, ash from cathode material and separators, and products of exothermal reactions and traces of anode graphite. It is observed that in the case of module 11 there are more dark-colored floccules than in the case of module 30, and there are more in the upper cathode than in the lower cathode. Therefore, it is concluded that module 11, in vertical arrangement, experiences higher temperature in the thermal runaway at the same SoC as module 30, which is in horizontal arrangement.
- Regarding the morphology, it is observed that in the case of the lower cathode of module 30 (horizontal arrangement) the particles are smaller compared to the upper cathode of module 30. This may be due to the higher temperature since it is more exposed. In the case of module 11 (vertical arrangement) there is no difference between the particle size of the upper cathode and the lower cathode.
- It is observed that in the case of modules 30 and 11 with a SoC of 68% after thermal runaway, the layered structure of the material was destroyed, the particles dispersed outside the original layered structure, and adhesion occurred. The positive electrode material (cathode) reacted at high temperature and decomposed. On the other hand, carbon particles from the negative electrode (anode) were get into the positive electrode (cathode) structure through the damaged diaphragm.
- In the lower cathode of module 30 there is a higher amount of fluorine, aluminum, manganese, phosphorus, nickel, and cobalt than in the upper cathode.
- Regarding module 11, a higher amount of aluminum and oxygen compound is observed, this may be since in this case the aluminum collector has been more damaged than in the case of module 30.
- The analysis of the cell anodes after the fire test, shows that the anode has peaks of oxygen and peaks of carbon, which indicates the formation of lithium carbonate (Li_2CO_3).
- It is observed that when the cell fails, the pressure caused by swelling due to outgassing leaves visible fractures in the cathode.
- Analysis of the stacked layer samples revealed interesting aspects of the interior of the investigated battery, including an additional separator layer in the tab area of the battery, and showed that the separator and bag were welded along the edge of the battery.
- When analyzing the structure, it is observed that in zone 3 the cell of module 11 on the outside and the cell of module 30 on the inside are more damaged.
- In both zone 1 (anode) and zone 2 (cathode), the cell of module 30 is more damaged than that of module 11 and in the case of zone 2.

The results of this study indicate that a more detailed structural analysis of the different layers of the cell (visualization of coatings, additional layers deposited due to the exothermic reaction, study of the pore size of the separator, among other characteristics) should be carried out to improve the identification of the material composition of each layer. On the other hand, the technique of obtaining the test samples is also important so that no impurities contaminate the sample.

Regarding the safety of the battery, the results of this study will allow to determine which arrangement and structure of the cells within the battery pack is safer against thermal runaway due to thermal failure. On the other hand, the identification of the chemical composition of each of the cell layers and of the compounds generated as a residue of a lithium-ion battery after a thermal abuse

test is very useful for the intervention of first responders, and to develop safe procedures to implement in response to accidents involving lithium-ion batteries.

Author Contributions: Conceptualization, A.O. and L.C.; data curation, A.O. and L.C.; formal analysis, A.O. and L.C.; funding acquisition, A.O. and L.C..; investigation, A.O. and L.C.; methodology, A.O. and L.C.; project administration, L.C.; resources, A.O. and L.C.; supervision, L.C.; writing—original draft, A.O. and L.C.; writing—review and editing, A.O. All authors have read and agreed to the published version of the manuscript.

Funding: University of Zaragoza: Industrial Doctorate (DI 4/ 2020).

Data Availability Statements: The data presented in this study are available on request from the corresponding author. The data are not publicly available due to restrictions privacy.

Acknowledgments: The authors are grateful for the support received through the Industrial Doctorate financed by the University of Zaragoza (DI 4/ 2020) and Instituto de Investigación sobre Vehículos, S.A. (Centro Zaragoza), in which the work presented in this article was framed.

Conflicts of Interest: The authors declare no conflict of interest.

References

1. Hyung-Joo Noh, Sungjune Youn, Chong Seung Yoon, Yang-Kook Sun (2013). Comparison of the structural and electrochemical properties of layered $Li[Ni_xCo_yMn_z]O_2$ (x=1/3, 0.5, 0.6, 0.7, 0.8 and 0.85) cathode material for lithium-ion batteries. Journal of Power Sources. Volume 233, 1 July 2013, Pages 121-130.
2. Electrek 2018. Available online: https://electrek.co/2018/06/16/tesla-model-s-battery-fire-investigating/ (accessed on 28 November 2023).
3. Yahoo!news 2019. Available online: https://sg.news.yahoo.com/tesla-car-catches-fire-hong-kong-parking-lot-050418281--finance.html?guccounter=1&guce_referrer=aHR0cHM6Ly93d3cuZ29vZ2xlLmNvbS8&guce_referrer_sig=AQAAAClpkmgR9urlu5KzzVB-y0uh0DW8ghCIrL9EdFrWSrIT8vBTETyCHsDA7mD5_1traEOgmIBOpuOZXf4YnfLD95g-yLPlIlLgysRGQE48TSCJ4CdwpZKHvgTWfNP0r98GLV4CHFC9g-qRRZo2c0GcQPZZ3X4LK_4Y66TUg90JdNlN (accessed on 28 November 2023).
4. CNN Business 2019. Available online: https://edition.cnn.com/2019/05/16/business/tesla-fire-battery-software-update/index.html#:~:text=Tesla%20is%20upgrading%20the%20battery,and%20improve%20their%20overall%20longevity (accessed on 28 November 2023).
5. Electrek 2023. Available online: https://electrek.co/2023/04/27/tesla-fire-police-believed-battery-arson/ (accessed on 28 November 2023).
6. Carnewschina 2023. Available online: https://carnewschina.com/2023/08/09/tesla-model-s-fire-in-sichuan/(accessed on 28 November 2023).
7. cbsnews 2023. Available online: https://www.cbsnews.com/sacramento/news/tesla-spontaneously-catches-fire-in-rancho-cordova-high-end-vehicle-scrap-yard/ https://carnewschina.com/2023/08/09/tesla-model-s-fire-in-sichuan/(accessed on 28 November 2023).
8. Sun, P., Bisschop, R., Niu, H. and Huang, X. (2020) A Review of Battery Fires in Electric Vehicles. Fire Technology, 56, 1361-1410.
9. P.G. Balakrishnan, R. Ramesh, T.P. Kumar (2006). Safety mechanisms in lithium-ion batteries. J. Power Sources 155 (2) (2006) 401–414.
10. Chen M, Yuen R, Wang J. An experimental study about the effect of arrangement on the fire behaviors of lithium-ion batteries. *J Therm Anal Calor* 2017; 129(1): 181–188.
11. Feng, X.; Ouyang, M.; Liu, X.; Lu, L.; Xia, Y.; He, X. Thermal Runaway mechanism of lithium ion battery for electric vehicles: A review. Energy Storage Mater. 2018, 10, 246–267.
12. H. Wang, E. Lara-Curzio, E.T. Rule, C.S. Winchester. Mechanical abuse simulation and thermal runaway risks of large-format Li-ion batteries J. Power Sources 342 (2017) 913–920.
13. Huang, P., Wang, Q., Li, K. et al. The combustion behavior of large scale lithium titanate battery. Sci Rep 5, 7788 (2015)
14. Y. Fu, S. Lu, K. Li, C. Liu, X. Cheng, H. Zhang, An experimental study on burning behaviors of 18650 lithium ion batteries using a cone calorimeter, J. Power Sources. 273 (2015) 216–222.
15. Chen, M.; Zhou, D.; Chen, X.; Zhang, W.; Liu, J.; Yuen, R.; Wang, J. Investigation on the Thermal Hazards of 18650 Lithium IonBatteries by Fire Calorimeter. J. Therm. Anal. Calorim. 2015, 122, 755–763.
16. X. Feng, M. Fang, X. He, M. Ouyang, L. Lu, H. Wang, M. Zhang, TR features of large format prismatic lithium ion battery using extended volume accelerating rate calorimetry, J. Power Sources 255 (2014) 294-301.

17. E.P. Roth, D.H. Doughty, Thermal abuse performance of high-power 18650 Li-ion cells.J. Power Sources 128 (2) (2004) 308–318.
18. Wang, Q., Sun, J., Yao, X., and Chen, C. (2006). Thermal behavior of lithiated graphite with electrolyte in lithium-ion batteries. J. Electrochem. Soc. 153, A329–A333.
19. S. Ma, M. Jiang, P. Tao, C. Song, J. Wu, J. Wang, T. Deng, W. Shang, Temperature effect and thermal impact in lithium-ion batteries: A review. Prog. Nat. Sci. 28 (6) (2018) 653–666.
20. S. Zhang. Problems and their origins of Ni-rich layered oxide cathode materials. Energy Storage Mater. 24 (2020) 247–254.
21. Peng Y, Yang L, Ju X, Liao B, Ye K, Li L, Cao B, and Ni Y. 2020. A comprehensive investigation on the thermal and toxic hazards of large format lithium-ion batteries with LiFePO4 cathode. Journal of Hazardous Materials 381:120916.
22. Wang, Q., Ping, P., Zhao, X., Chu, G., Sun, J. and Chen, C. (2012) Thermal Runaway Caused Fire and Explosion of Lithium Ion Battery. Journal of Power Sources, 208, 210-224.
23. Bai, F, Chen, M, Song, W, Feng, Z, Li, Y & Ding, Y 2017, 'Thermal management performances of PCM/water cooling-plate using for lithium-ion battery module based on non-uniform internal heat source', Applied Thermal Engineering, vol. 126, pp. 17-27.
24. M. Garg, T.R. Tanim, C.D. Rahn, H. Bryngelsson, N. Legnedahl. Elevated temperature for life extension for lithium ion power cells. Energy 159 (2018). Pages 716-723.
25. N.E. Galushkin, N.N. Yazvinskaya, D.N. Galushkin. Mechanism of gases generation during lithium-ion batteries cycling. J. Electrochem. Soc. 166 (6) (2019) A897–A908.
26. Wang, G., Kong, D., Ping, P., He, X., Lv, H., Zhao, H., Hong, W., 2023. Modelingventing behavior of lithium-ion batteries during thermal runaway propa-gation by coupling CFD and thermal resistance network. Appl. Energy 334,12066.
27. Z. Wang, N. Mao, F. Jiang. Study on the effect of spacing on thermal runaway propagation for lithiu-ion batteries. Journal of Thermal Analysis and Calorimetry (2020).
28. J. Fang, J. Cai, X. He. Experimental study on the vertical thermal runaway propagation in cylindrical Lithium-ion batteries: Effects of spacing and state of charge. Applied Thermal Engineering Volume 197, October 2021, 11739.
29. X. Feng, J. Sun, M. Ouyang, F. Wang, X. He, L. Lu, H. Peng, Characterization of penetration induced thermal runaway propagation process within a large format lithium ion battery module, J. Power Sour. 275 (2015) 261–273.
30. X. Feng, L. Lu, M. Ouyang, J. Li, X. He, A 3D thermal runaway propagation model for a large format lithium ion battery module, Energy 115 (2016) 194–208.
31. C.F. Lopez, J.A. Jeevarajan, P.P. Mukherjee, Experimental analysis of thermal runaway and propagation in lithium-ion battery modules, J. Electrochem. Soc. 162 (2015) A1905–A1915.
32. S. Wilke, B. Schweitzer, S. Khateeb, S. Al-Hallaj, Preventing thermal runaway propagation in lithium ion battery packs using a phase change composite material: An experimental study, J. Power Sour. 340 (2017) 51–59.
33. J. Lamb, C.J. Orendorff, L.A.M. Steele, S.W. Spangler, Failure propagation in multi-cell lithium ion batteries, J. Power Sour. 283 (2015) 517–523
34. S. Gao., X. Feng, L. Lu, N. Kamyab, J. Du, P. Comsn, R. E. White, M. Ouyang. An experimental and analytical study of thermal runaway propagation in a large format lithium ion battery module with NMC pouch-cells in parallel. 2019, International Journal of Heat and Mass Transfer Volume 135, June 2019, Pages 93-103
35. G. Kovachev, H. Schröttner, G. Gstrein, L. Aiello , I. Hanzu, H. Martin R. Wilkening , A. Foitzik, M. Wellm, W. Sinz and C. Ellersdorfer. "Analytical Disection of an Automotive Li-Ion Pouch Cell". Batteries 2019, 5, 67; doi:10.3390/batteries5040067.
36. X. Zhu, Z. Sun, Z. Wang, H. Wang, N. Lin, C. Shan. Thermal runaway in commercial lithium-ion cells under overheating condition and the safety assessment method: Effects of SoCs, cathode materials and packaging forms. Journal of Energy Storage 68 (2023) 107768.
37. Arora, P.; Zhang, Z. Battery Separators. Chem. Rev. 2004, 104, 4419–4462.
38. Luo M. J., Guo Y. Z. and Kang J. Q. 2018. Ternary-material lithium-ion battery SOC estimation under various ambient temperature. Ionics 24 1-11.
39. Wang J. L., Wu H. L. and Cui Y. H. 2018. A new class of ternary compound for lithium-ion battery: from composite to solid solution Acs. Appl. Mater. Interfaces. 10 1-6.

40. H. J. Xie et al 2021. Lithium-Ion Battery Thermal Runaway Electro-Thermal Triggering. Method and Toxicity Analysis. IOP Conf. Ser.: Earth Environ 2021. Sci. 701 012007.
41. D. P. Finegan, M. Scheel, J. B. Robinson, B. Tjaden, M. D. Michiel, G. Hinds, D. J. L. Bretta and P. R. Shearing. Investigating lithium-ion battery materials during overcharge-induced thermal runaway: an operando and multi-scale X-ray CT study†. 2016, PPC, Royal Society of Chemestry. DOI: 10.1039/c6cp04251a.